PCCP

PAPER

View Article Online
View Journal | View Issue

Check for updates

Cite this: *Phys. Chem. Chem. Phys.*, 2020, **22**, 5647

Holistic approach to chemical degradation of Nafion membranes in fuel cells: modelling and predictions†

Philipp Frühwirt,[a] Ambrož Kregar,[ab] Jens T. Törring,[a] Tomaž Katrašnik[b] and Georg Gescheidt*[a]

The state of health of polyfluorinated sulfonic-acid ionomer membranes (*e.g.* Nafion®) in low-temperature proton exchange membrane fuel cells (LT-PEMFCs) is negatively influenced by degradation phenomena occurring during their operation. As a consequence, the performance and durability of the membrane are decreased. In this article, we focus on simulating and predicting chemical membrane degradation phenomena using a holistic zero-dimensional kinetic framework. The knowledge of chemical degradation mechanisms is widely spread. We have collected and evaluated an extensive set of chemical mechanisms to achieve a holistic approach. This yields a set of 23 coupled chemical equations, which provide the whole cause and effect chain of chemical degradation in LT-PEMFCs (based on the Fenton reaction between Fe^{2+} and H_2O_2 *via* the attack of hydroxyl radicals on the membrane, loss of ionomer moieties and emission of fluoride). Our kinetic framework allows the reproduction of experimentally accessible data such as fluoride emission rates and concentrations of ionomer moieties (from both *in situ* and *ex situ* tests). We present an approach, which allows estimations of the membrane lifetime based on fluoride emission rates. In addition, we outline the demetallation of Fe–N–C catalysts as a source of additional harmful iron species, which accelerate chemical membrane degradation. To demonstrate the expandability and versatility of the kinetic framework, a set of five chemical equations describing the radical scavenging properties of cerium agents is coupled to the main framework and its influence on membrane degradation is analysed. An automated solving routine for the system of coupled chemical equations on the basis of the chemical kinetic simulation tool COPASI has been developed and is freely accessible online (http://ptc-pc-139.tugraz.at/cgi-bin/Membrane_Degradation/).

Received 8th September 2019,
Accepted 3rd February 2020

DOI: 10.1039/c9cp04986j

rsc.li/pccp

Open Access Article. Published on 26 February 2020. Downloaded on 2/15/2026 7:49:42 AM.
This article is licensed under a Creative Commons Attribution-NonCommercial 3.0 Unported Licence.

Introduction

In 2014, two-thirds of the world's total carbon dioxide emissions originated from the industry, electricity/heat and transport sectors. In the US and Europe, transportation accounted for about one-third of the total greenhouse gas emissions in that year.[1] Approaches to tackle the decarbonisation in this sector are under development or even commercialised – *e.g.* hybrid electric vehicles (combination of conventional internal combustion engine and electric power engine), battery electric vehicles, fuel cell electric vehicles and fuel cell hybrid electric vehicles. Except for hybrid electric vehicles, they do not produce pollutants during operation. Provided that the electric power or fuel is produced in an ecologically sound manner from renewable sources, they can provide a CO_2 neutral means of transportation. Vehicles powered by fuel cells (FCs) are superior in comparison to those relying on batteries when it comes to range and time required for recharging. However, the fuel cell technology suffers from a different type of problem – the restricted durability of the fuel cell components such as the membrane and the catalyst, and hence a limited long-term reliability of the fuel cells.[2–4]

One of the most frequently used types of FCs in the automotive sector are proton exchange membrane fuel cells (PEMFCs) operated at temperatures between 60 °C and 100 °C.[2,5] These low-temperature PEMFCs usually comprise a polyfluorinated sulfonic-acid (PFSA) ionomer as the membrane (*e.g.* Nafion®). The chemical composition of Nafion® is depicted in Fig. 1. Due to the

[a] *Institute of Physical and Theoretical Chemistry, Graz University of Technology, Stremayrgasse 9, 8010 Graz, Austria. E-mail: g.gescheidt-demner@tugraz.at*
[b] *Faculty of Mechanical Engineering, University of Ljubljana, Aškerčeva 6, 1000 Ljubljana, Slovenia*

† Electronic supplementary information (ESI) available: General scheme of the used automated solving routine, examples for input and output files, implementation of the model in Mathematica, Mathematica script. See DOI: 10.1039/c9cp04986j

Open Access Article. Published on 26 February 2020. Downloaded on 2/15/2026 7:49:42 AM.
This article is licensed under a Creative Commons Attribution-NonCommercial 3.0 Unported Licence.

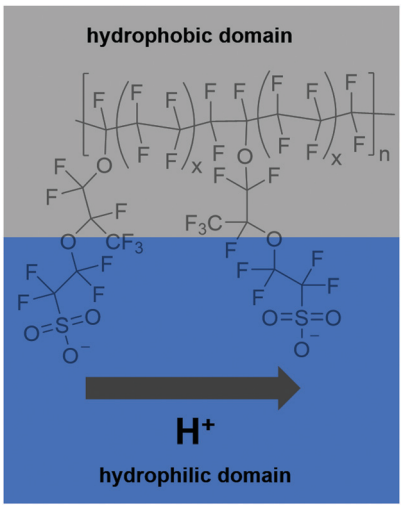

Fig. 1 Chemical composition of Nafion® 117 (x = 6.5). The protons are conducted in the hydrophilic domain (blue box) while the hydrophobic backbone (grey box) ensures mechanical stability of the membrane.

amphiphilic nature of the membrane, the conduction of the protons from the anode to the cathode side is ensured. This function is indispensable for the overall functionality of the fuel cell system. Thus, all degradation processes affecting the membrane reduce the efficiency of the fuel cell and considerably impact the reliability and durability of the system as a whole.[5–7]

Membrane integrity is affected by chemical, thermal and mechanical degradation.[8] Here, we focus on the chemical membrane degradation in low-temperature PEMFCs. An excellent discussion of various degradation phenomena can be found in the reviews by Borup *et al.*,[6] Kusoglu and Weber[7] as well as Zatoń *et al.*[5] Many mechanisms and the corresponding chemical equations[9–13] and kinetic details[14–28] have been reported. Based on that, several chemical degradation models[29–36] have been already presented. This knowledge, however, is spread in physically, chemically and technologically oriented context. Here we present an extensive picture of chemical degradation combining established data to describe chemical conversions in a Nafion® membrane. We use a zero-dimensional (0D) chemical reactor model comprising a set of 23 coupled chemical equations. This powerful model allows monitoring and prediction of experimentally accessible data like time traces of chemical species involved[33] and fluoride emission rates (FERs).[35–37] Furthermore, we discuss the implications of iron containing ORR catalysts[38–40] for membrane degradation and the use of cerium agents[41–47] as radical scavengers to protect the chemical integrity of the membrane.

Modelling approach

Our kinetic framework and the assumptions of the model are based on fragmented knowledge spread across several chemical and technical publications. Accordingly, we, in the first instance, provide an overview of the state-of-the-art in terms of chemical membrane degradation.

Formation of radical species

Experimental evidence that radical species are formed during the operation of the fuel cell was presented by Panchenko *et al.*[48] By operating a miniature fuel cell within an electron paramagnetic resonance (EPR) spectrometer, radical species which arose from the electrode carbon material were detected. A similar setup was used by Danilczuk *et al.*[49] to detect reactive oxygen species (ROS) such as hydroxyl ($^{\bullet}$OH), hydroperoxyl ($^{\bullet}$OOH) and additionally, hydrogen ($^{\bullet}$H) and membrane-derived radical fragments after capturing them with a spin-trap.

The mechanism behind the formation of these species is a matter of debate. Under typical operation conditions oxygen is reduced at the cathode in the oxygen reduction reaction (ORR). This can happen *via* different reaction routes – either a direct reduction involving 4 electrons (eqn (1)) or two consecutive two-electron reductions (eqn (2) and (3)) forming hydrogen peroxide (H_2O_2) as an intermediate:[50,51]

$$O_2 + 4e^- + 4H^+ \rightleftarrows 2H_2O \quad E^0 = 1.229\ \text{V} \qquad (1)$$

$$O_2 + 2e^- + 2H^+ \rightleftarrows H_2O_2 \quad E^0 = 0.695\ \text{V} \qquad (2)$$

$$H_2O_2 + 2e^- + 2H^+ \rightleftarrows 2H_2O \quad E^0 = 1.763\ \text{V} \qquad (3)$$

By equipping the membrane with Pt microelectrodes, Liu and Zuckerbrod[52] were able to detect micromolar concentrations of H_2O_2 in the membrane during operation (60 °C, open circuit voltage (OCV) conditions). Nevertheless, the formation of H_2O_2 is not confined to the cathode side. During operation of the fuel cell, oxygen can diffuse to the anode side, where H_2O_2 is also formed. A dependence of $[H_2O_2]$ on the thickness of the membrane was also observed – the thinner the membrane, the higher $[H_2O_2]$. This is most likely connected to the increased O_2 crossover in thinner membranes.[52] Similar results were obtained by Chen and Fuller.[53] Shah *et al.*[30] calculated $[H_2O_2]$ in the membrane for different operating conditions (voltage, temperature) – the highest values were found to be near or in the anode catalyst layer (up to 3.5 mM) while the value on the cathode side stayed below 0.5 mM for 60 °C and OCV. Simulations by Wong and Kjeang[34] indicate $[H_2O_2]$ of about 1.5 mM in the membrane under OCV conditions. Inaba *et al.*[54] supposed that due to the elevated boiling point of H_2O_2 compared to that of water the concentration of H_2O_2 could be increased when the fuel cell is operated under low humidity conditions.

H_2O_2 is not a strong enough oxidant to attack the ionomer directly and is, therefore, characterised by a relatively long lifetime within the fuel cell. This leads to a diffusion length of H_2O_2 in the mm to cm range, which is large compared to the typical membrane thickness (in the μm range).[31] Under certain conditions, though, H_2O_2 is highly active in oxidizing organic substrates (like the fuel cell membrane) – a fact which has been known for more than hundred years. In 1894, Fenton discovered that a mixture of H_2O_2 and ferrous salts effectively reacts with tartaric acid.[55] The reaction between ferrous ions and H_2O_2 is known as the Fenton reaction:[56,57]

$$Fe^{2+} + H_2O_2 + H^+ \rightleftarrows Fe^{3+} + {}^{\bullet}OH + H_2O \qquad (4)$$

 This journal is © the Owner Societies 2020

Open Access Article. Published on 26 February 2020. Downloaded on 2/15/2026 7:49:42 AM.
This article is licensed under a Creative Commons Attribution-NonCommercial 3.0 Unported Licence.

Furthermore, the emerging species are also involved in further redox reactions leading to the formation of additional ROS and redox recycling of the active ferrous ion:[58,59]

$$Fe^{3+} + H_2O_2 \rightleftarrows Fe^{2+} + {}^{\bullet}OOH + H^+ \quad (5)$$

$$Fe^{2+} + {}^{\bullet}OH + H^+ \rightleftarrows Fe^{3+} + H_2O \quad (6)$$

$$Fe^{2+} + {}^{\bullet}OOH + H^+ \rightleftarrows Fe^{3+} + H_2O_2 \quad (7)$$

$$Fe^{3+} + {}^{\bullet}OOH \rightleftarrows Fe^{2+} + H^+ + O_2 \quad (8)$$

Pozio *et al.*[57] demonstrated that stainless steel (type SS316L) end plates serve as a source of iron contaminants in fuel cells. When using aluminium (Al) end plates *in operando* the average fluoride concentration measured in the cathode water was only about 1/10 of that with stainless steel end plates. For the anode side a reduction in fluoride emission by 60% was observed when switching from SS316L end plates to Al end plates. In addition, a decrease in Fe concentration in the cathode water from about 600 ppb (for SS316L) to less than 100 ppb (for Al) was also evident. For the anode water in the case of SS316L end plates, a Fe concentration of 925 ppb was determined. Papadias *et al.*[60] found a total ion release rate of about 0.4 μg cm^{-2} h^{-1} in the range of 0 to 1 V for stainless steel (type SS316L) bipolar plates. 90% of all released ions were Fe and Ni.

Not only the end plates used in fuel cells, but also the membrane material might contribute to the contamination of the fuel cell with iron. Coms *et al.*[61] estimated the BOL (begin of life) concentration of iron to be 5 to 10 ppm. Liu *et al.*[62] attributed an iron concentration of 5 ppm to an as-received NE112 ionomer. Due to the anionic nature of the sulfonic acid head groups Nafion® is known to immobilise iron ions,[63] which could even lead to an accumulation of iron within the membrane during operation. Andersen[64] observed in swelling–dehydration experiments with Nafion® 212 that the ionomer tends to have higher selectivity for high-valence cations (like Fe^{3+}), which then replace protons and negatively impact the proton conductivity of the ionomer and its thermochemical properties.[7]

The observation that ferrous ions accelerate the membrane degradation is actively employed in *ex situ* degradation tests (so-called Fenton tests)[65–67] and also *in situ* tests[41,62] to assess the durability of membrane materials. Other transition metal ions such as Ti^{3+},[66] Co^{2+} [68,69] or Cu^{+} [70–72] are also known to convert H_2O_2 to ROS like $^{\bullet}OH$ and $^{\bullet}OOH$.

In addition to the formation of radical species *via* hydrogen peroxide as an intermediate, radicals can also be formed directly on platinum surfaces. Density functional theory (DFT) calculations by Atrazhev *et al.*[73] show that formation of $^{\bullet}OH$ might be possible under conditions where the oxygen reduction is prevented by the presence of other adsorbed species. In close vicinity to other Pt particles (*e.g.* in the electrode) $^{\bullet}OH$ might be destroyed effectively before reaching the polymer membrane, as for the adsorption of hydroxyl radicals no activation barrier at any potential is calculated.[73] Despite the decreased selectivity for $^{\bullet}OH$ to attack the membrane in Pt-rich environments, Pt particles deposited into a PFSA membrane increased the FER compared to the untreated membrane.[74] Whether dispersed platinum particles catalyse the formation of radicals or act as scavengers and protect the membrane from radical attack is a function of the metal loading in the membrane. At higher platinum levels (30 to 50 mol%) radical scavenging is predominant while at 10 mol% ($n_{Pt}/n_{membrane}$) this is outweighed by the generation of radicals.[75]

Due to the sluggish kinetics of the ORR, high amounts of Pt or Pt alloys need to be used at the cathode side to efficiently catalyse the oxygen reduction. To reduce or avoid the use of the precious noble metal, alternatives such as non-precious metal catalysts (NPMCs) have been developed. Among these are metal/nitrogen/carbon (M–N–C) catalysts, where the metal is mostly iron. Although they are highly active in catalysing the oxygen reduction reaction, there is still room for improvement in terms of durability and stability.[38] A lifetime-limiting factor for Fe–N–C catalysts is the Fe demetallation in acidic media (such as the PEMFC). Depending on the synthesis of the catalyst, inactive Fe particles (in addition to the active FeC_xN_y centres) remain at the surface, which cannot be completely removed by acid washing and lead to iron leaching *in operando*.[39] A recent study by Chenitz *et al.*[40] showed that demetallation at the catalytic Fe–N_4 centres of a Fe–N–C catalyst (NC_Ar + NH_3) due to the flux of water in the micropores of the catalyst is also possible providing an additional source of iron species.

Overview of degradation mechanisms

Regardless of the formation mechanism of radical species, Nafion® ionomers offer in principle four different points of attack for $^{\bullet}OH$ or $^{\bullet}H$: (1) carboxylic acid (–COOH) end groups in the main chain (unzipping mechanism), (2) the sulfonic acid head groups (–SO_3H), (3) ether groups in the side chain and finally (4) the tertiary carbons found in both side chain and main chain (Fig. 2).[5]

Main chain degradation mechanism. The main chain degradation mechanism according to Curtin *et al.*[9] relies on fragile end groups (*e.g.* carboxylic acid moieties)[76] in the backbone (BB) of Nafion® formed during the manufacture of the

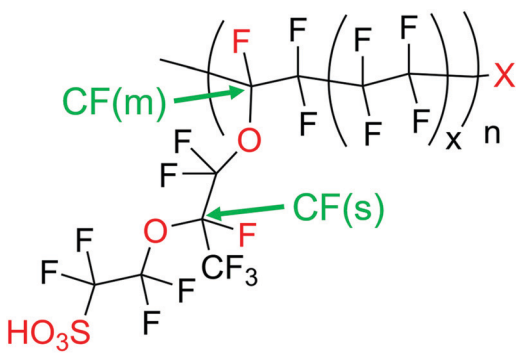

Fig. 2 Chemical composition of Nafion® 117 (x = 6.5) as an example for a commonly used PFSA. The points of attack for radical species are marked in red and the green labels represent the tertiary carbon atoms. X stands for a weak end group like –COOH.

Open Access Article. Published on 26 February 2020. Downloaded on 2/15/2026 7:49:42 AM.
This article is licensed under a Creative Commons Attribution-NonCommercial 3.0 Unported Licence.

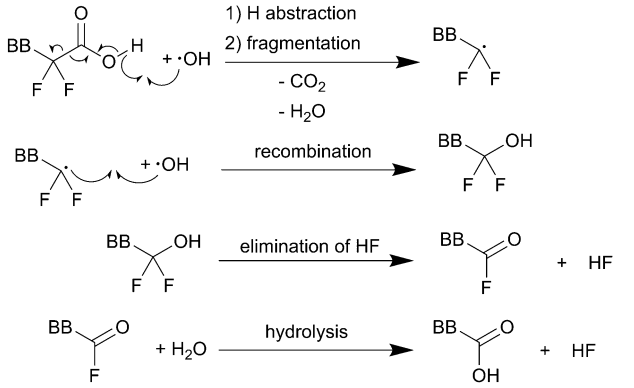

Scheme 1 Main chain degradation mechanism as proposed by Curtin *et al.*[9] BB represents the backbone of the PFSA ionomer. Single barbed arrows indicate the formation of new chemical bonds and homolytic cleavage of bonds.

membrane (see Scheme 1). The mechanism is initiated by an abstraction of the carboxylic hydrogen by •OH followed by the fragmentation of the intermediate radical species to CO_2 and BB–CF_2•. After recombination with another •OH the formed primary alcohol undergoes elimination of hydrogen fluoride (HF). The product (acid fluoride) is prone to hydrolysis to give another carboxylic acid moiety and the cycle restarts. For each degradation cycle (loss of one –COOH moiety and conversion of the adjacent CF_2 unit to a new –COOH group) two •OH are needed to form two HF molecules. Hence, a linear dependence of fluoride emission on the number of COOH groups can be expected here, which is corroborated by the results obtained from *ex situ* Fenton tests by Schwiebert *et al.*[77] Zhou *et al.*[78] performed degradation experiments with small molecule analogues for Nafion® and found that model compounds with carboxylic acid terminals degrade one order of magnitude faster than molecules without COOH groups.

Thermodynamic driving force for hydrogen abstraction is the formation of a strong O–H bond (namely that of H_2O) with an experimental bond enthalpy (ΔH_{298}) of 497 kJ mol^{-1} while cleaving the weaker O–H bond of the carboxylic acid (computed bond enthalpy of 426 kJ mol^{-1} for CF_3COOH).[10]

The number of unprotected groups can be greatly reduced by chemical stabilisation techniques (*e.g.* conversion of –COOH to –CF_3 by treatment with fluorine).[9,79] Cipollini[79] found lower FERs for treated Nafion® membranes in Fenton degradation tests. But the same author also observed that *in operando* (90 °C, 30% relative humidity, anode: H_2 + 5% O_2, cathode: O_2), these differences in FER values between untreated and treated ionomers vanished. These experimental observations indicate the presence of other degradation mechanisms under fuel cell conditions.[79]

Further experimental evidence for the unzipping mechanism was presented by Danilczuk *et al.*[80] The stability of different polyfluorinated membranes (Nafion®, stabilised Nafion®, 3M ionomer and Aquivion®) was investigated by spin-trapping EPR spectroscopy. •OH was generated by photolysis of H_2O_2 in the presence of the ionomers and then trapped by using DMPO

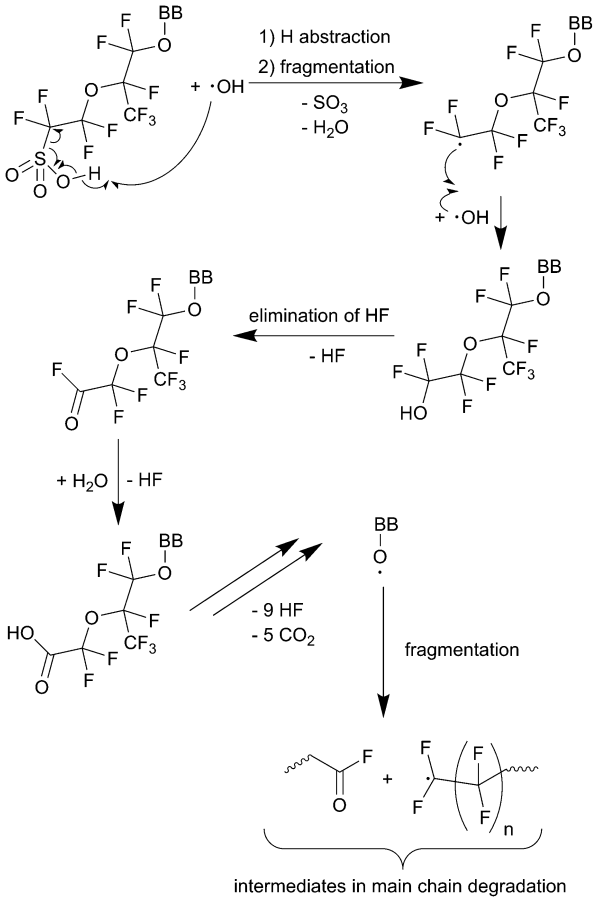

Scheme 2 Side chain degradation mechanism as proposed by Ghassemzadeh *et al.*[11] BB represents the backbone of the PFSA ionomer. Single barbed arrows indicate the formation of new chemical bonds and homolytic cleavage of bonds.

(5,5-dimethyl-1-pyrroline *N*-oxide). Besides the detection of the expected DMPO–OH radical adduct, carbon-centred radical intermediates were also established for all ionomers. For the 3M and the Aquivion® ionomer it was concluded that the observed radical adduct is a result of an attack of •OH on the COOH moieties of the polymers. For Nafion® and stabilised Nafion® another carbon-centred radical species was detected, which was attributed to a side-chain-derived radical.[80]

Attack at the sulfonic acid moiety. Attack on the sulfonic acid moiety located in the side chain (SC) was proposed by Ghassemzadeh *et al.*[11] (Scheme 2) based on the detection of the end-chain radical SC–OCF_2CF_2• upon UV irradiation of Nafion® in the presence of Fe(III) or Fe(II) and H_2O_2.[81,82] DFT calculations for CF_3SO_3H show that a bond enthalpy of only 236 kJ mol^{-1} can be ascribed to the C–S bond rendering it the weakest bond among all bonds in the side chain.[10]

The O–H bond of the sulfonic group involved in the first reaction in Scheme 2 features a bond enthalpy of 406 kJ mol^{-1} (computed for CF_3SO_3H)[10] making the hydrogen abstraction by •OH energetically favourable. The following steps finally lead to an unstable alkoxy radical (BB–O•) which is then inevitably converted to an acid fluoride and a BB–CF_2• radical – both

 This journal is © the Owner Societies 2020

Open Access Article. Published on 26 February 2020. Downloaded on 2/15/2026 7:49:42 AM.
This article is licensed under a Creative Commons Attribution-NonCommercial 3.0 Unported Licence.

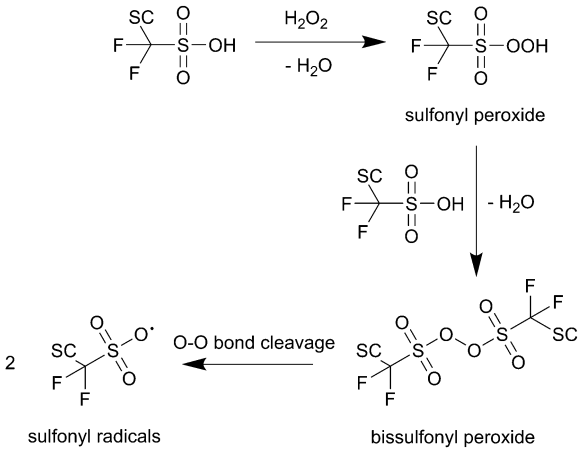

Scheme 3 Formation of sulfonyl radicals *via* peroxide intermediates as proposed by Coms.[10] SC represents the side chain of the ionomer.

involved in the main chain unzipping process, too. As an intermediate in the first step a sulfonyl radical (SC–$OCF_2CF_2SO_3^{\bullet}$) is postulated,[81] which can also be generated by another mechanism involving H_2O_2 as an oxidant for the sulfonic acid (see Scheme 3).[10] The intermediate sulfonyl peroxide can react with another sulfonic acid to form bissulfonyl peroxide, whose O–O bond is finally cleaved to yield two sulfonyl radicals. Again, the cleavage of the weak C–S bond leads to SC–$OCF_2CF_2^{\bullet}$ and SO_3.[10]

Ether cleavage mechanism. Not only the sulfonic acid head group is susceptible to radical attacks, also the ether moiety in the side chain should be considered as a point of attack by radicals, as proposed by Ghassemzadeh *et al.*[12,13] A Nafion® 211 membrane was subjected to a Fenton test and the concentrations of the fluorine-containing membrane units were monitored by ^{19}F MAS NMR (magic angle spinning nuclear magnetic resonance) spectroscopy. The highest decrease in concentration (up to 15% over 48 h) was observed for the two CF_2 groups adjacent to the hydrophilic head group.[12] Similar results were obtained when using an electron beam to irradiate an aqueous solution of H_2O_2 in the presence of Nafion® 211.[13] This mechanism is further supported by EPR investigations by Danilczuk *et al.* showing that ionomers with shorter side chains (3M and Aquivion®) are characterised by a higher stability towards the radical attack of $^{\bullet}OH$ compared to (stabilised) Nafion®.[80]

The mechanism depicted in Scheme 4[13] starts with a radical-initiated ether cleavage on the side chain, which can happen from both sides of the ether oxygen leading to different side chain fragments, which could be detected by ^{19}F NMR. By using attenuated total reflection Fourier transform infrared spectroscopy (ATR-FTIR) the presence of C=O bonds could be established.[13]

Attack at the tertiary carbons. So far, all discussed degradation procedures rely on the attack of ROS. Beyond that, $^{\bullet}OH$ also tends to react with other H donors such as molecular hydrogen giving rise to hydrogen radicals:[83]

$$H_2 + {}^{\bullet}OH \rightleftarrows {}^{\bullet}H + H_2O \quad (9)$$

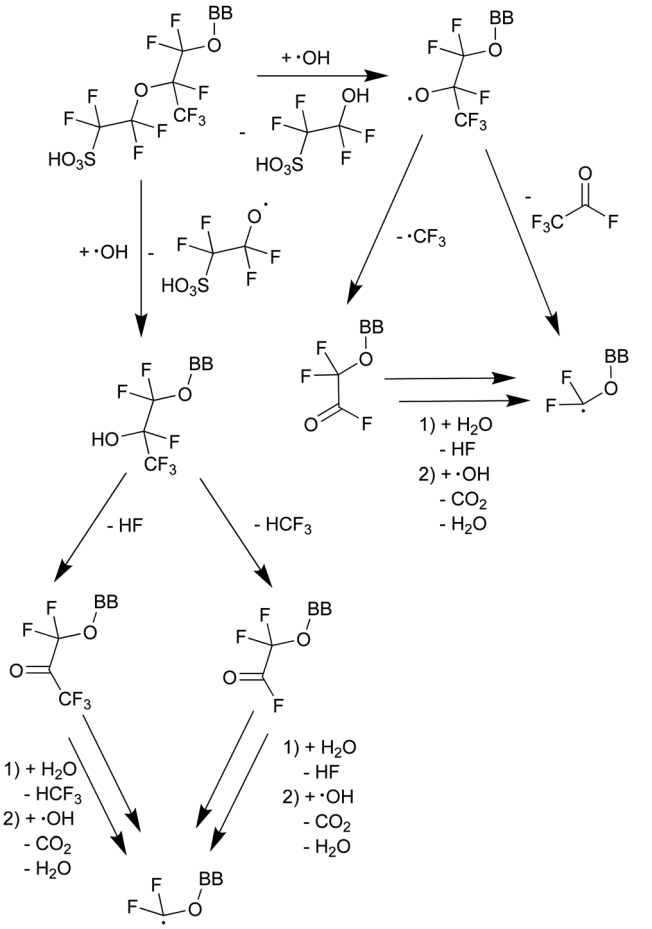

Scheme 4 Proposed mechanism of ether cleavage with subsequent fragmentation and side-chain unzipping.[13] BB represents the backbone of the PFSA ionomer.

As $^{\bullet}H$ is produced along with ROS like $^{\bullet}OH$ and $^{\bullet}OOH$ under fuel cell conditions,[49] it is difficult to study the impact of $^{\bullet}H$ on membrane degradation *in situ.* Ghassemzadeh *et al.*[13] were able to generate $^{\bullet}H$ selectively by irradiating an aqueous H_2SO_4 solution with an electron beam in the presence of Nafion® 211. Their results indicate that the points of attack for $^{\bullet}H$ are the tertiary C–F bonds located on the main and side chain (see Fig. 2). Based on that, a degradation mechanism involving just $^{\bullet}H$ was proposed. In principle, both tertiary C–F bonds are points of attack for the highly reactive $^{\bullet}H$ which finally leads to the fragmentation of the side chain at the tertiary carbons.[13] These findings are corroborated by DFT calculations[10,84] which demonstrate that the bond enthalpy of C–F bonds is the lowest for tertiary carbons. Based on the bond strengths (primary C–F: $\approx$ 520 kJ mol^{-1}; secondary C–F: $\approx$ 480 kJ mol^{-1}; tertiary C–F: $\approx$ 440 kJ mol^{-1}) and HF (571 kJ mol^{-1}) fluorine abstractions from any position of the Nafion® structure should be thermochemically favourable, though only abstractions at secondary and tertiary C–F bonds are estimated to be kinetically feasible.[10]

One should bear in mind that this mechanism is strictly valid only in a system where just $^{\bullet}H$ as radical species is present. Under fuel cell conditions, a synergetic cooperation

Open Access Article. Published on 26 February 2020. Downloaded on 2/15/2026 7:49:42 AM.
This article is licensed under a Creative Commons Attribution-NonCommercial 3.0 Unported Licence.

of the ROS and •H should be expected resulting in a more complicated degradation process. •H might activate the side chains for following attacks by ROS.

Previously published modelling approaches

On the basis of the degradation mechanisms discussed above several modelling approaches comprising membrane degradation phenomena[29–36] have been published. The model by Xie and Hayden[29] does not concentrate on the formation of radical species; yet it is possible to distinguish between two possibilities for initiation of PFSA degradation – either at the weak end groups of the main chain or at the side chains. In addition, it is impossible to deduce FERs from the model. A kinetic framework to describe the formation of H_2O_2 and ROS was provided in an extensive one-dimensional model of Shah *et al.*[30] Gubler *et al.*[31] presented a more comprehensive kinetic framework. With their zero-dimensional chemical reactor model comprising rate constants at room temperature they were able to estimate the quasi-steady state concentrations of •H, •OH and •OOH. FERs for *ex situ* Fenton and under fuel cell operation conditions after extrapolation to 90 °C were predicted. For the Fenton tests the agreement of the calculated FER with literature data was satisfying; however, the FER for *in situ* conditions was 2 to 3 orders of magnitude lower than the experimental results.

Both the models of Shah *et al.*[30] and Gubler *et al.*[31] rely on the main chain unzipping mechanism as the major membrane degradation mechanism, yet improved chemical post-treatment effectively decreased the number of weak end groups in PFSA ionomers.[79] Ghelichi *et al.*[32] used a similar kinetic framework to that of Gubler *et al.*[31] (rate constants at 80 °C instead of room temperature) in their coarse-grained degradation model dividing the PFSA structure into backbone, trunk and head group units. Radical concentrations were calculated following a steady-state approach neglecting the effects of the PFSA ionomer as a sink for radical species. The rate constants for the unzipping reaction and head group dissociation were derived from fitting analytical expressions to experimental data. For both the unzipping and the head group dissociation rate constant a good agreement with rate constants for model compounds determined by Dreizler and Roduner[20] was achieved. However, the rate constant for head group dissociation is dependent on the data used for fitting.[32]

Similar to Ghelichi *et al.*,[32] the approach by Wong and Kjeang[33] is also based on the degradation of the side chain and features the radical ether cleavage (shown in Scheme 4) as the initiation step of ionomer destruction. Even though the kinetic framework for radical formation only comprises the Fenton reaction and all reaction constants are given for room temperature, trends observed in *in situ* tests can be well reproduced with their model. The kinetic framework[33] was expanded in a later publication by Wong and Kjeang.[34] An analogue model was presented recently by Singh *et al.*,[35] being extended by regarding the temperature dependence of the Fenton reaction and an iron redox cycle, which is established by the reaction of ferric ions with hydrogen radicals.

A recent publication by Futter *et al.*[36] features an extensive radical reaction framework similar to the ones already presented.[30–32,34] Furthermore, the degradation reactions displayed in this model are based on the coarse-grained approach,[32] with an excellent agreement with experimental data from accelerated stress tests.

Modelling framework

In the following paragraphs our modelling framework is described (for schematic explanation see Scheme 5), which merges and expands the hitherto published ones.[30–36] A combination of ionomer degradation reactions[33–35] (see Scheme 6) with basic radical chemistry[14–28] leads to a system of 23 coupled chemical equations (see Table 1). This set of equations is then solved by an automatisation routine based on the freely available kinetic simulation program COPASI.[85] This allows predictions of fluoride emission rates and concentration traces of ionomer moieties and degradation products.

Our model relies on the following assumptions:

1. An isotherm zero-dimensional chemical reactor for the ionomer membrane. This model is characterised by uniform distribution of all involved chemical species over the whole reaction volume, which is equal to the membrane volume. Hence, no diffusion of species is observed. For highly reactive species such as •OH diffusion can indeed be neglected, as diffusion length in the nm range is estimated,[31] which is 3 orders of magnitude lower than the average thickness of the PFSA ionomer membrane. Once formed, the •OH radicals react with other species in close vicinity, and thus the damage induced by the radical attack can be considered as highly localised.

2. Besides •OH, the generation of •OOH and •H is also covered in the model, though their involvement in chemical membrane degradation is neglected. Due to the relatively low enthalpy of the O–H bond in H_2O_2 (366 kJ mol^{-1}) hydrogen abstraction from PFSA ionomers by •OOH radicals is thermodynamically highly unfavoured.[10] Nevertheless, the possibility of a recombination of •OOH with carbon-centred radicals formed during the degradation cannot be ruled out. Gubler *et al.*[31] argued that, despite the low steady-state concentration of •H at room temperature in the presence of ionomer (2 orders of magnitude lower than •OH), •H might have a considerable effect on the membrane degradation; however due to the lack of kinetic data, its influence cannot be evaluated by the model.

3. The primary source of ROS is assumed to be the reactions of H_2O_2 and both the ferrous (R_1; Fenton reaction) and ferric ions (R_2) and to a small extent the homolytic cleavage of the O–O bond in H_2O_2 (R_6). All other sources of ROS and hydrogen radicals (*e.g.* formation at Pt particles[73–75]) are neglected in the model. In addition, the potential-dependent redox recycling of iron species[34] in the membrane is not taken into account.

4. Although protons are involved in some of the chemical reactions, their rates are basically independent of the pH. Accordingly, pH effects[20] are not considered.

5. We consider the changes in concentration due to the swelling of the ionomer membrane[34] as negligible.

Open Access Article. Published on 26 February 2020. Downloaded on 2/15/2026 7:49:42 AM.
This article is licensed under a Creative Commons Attribution-NonCommercial 3.0 Unported Licence.

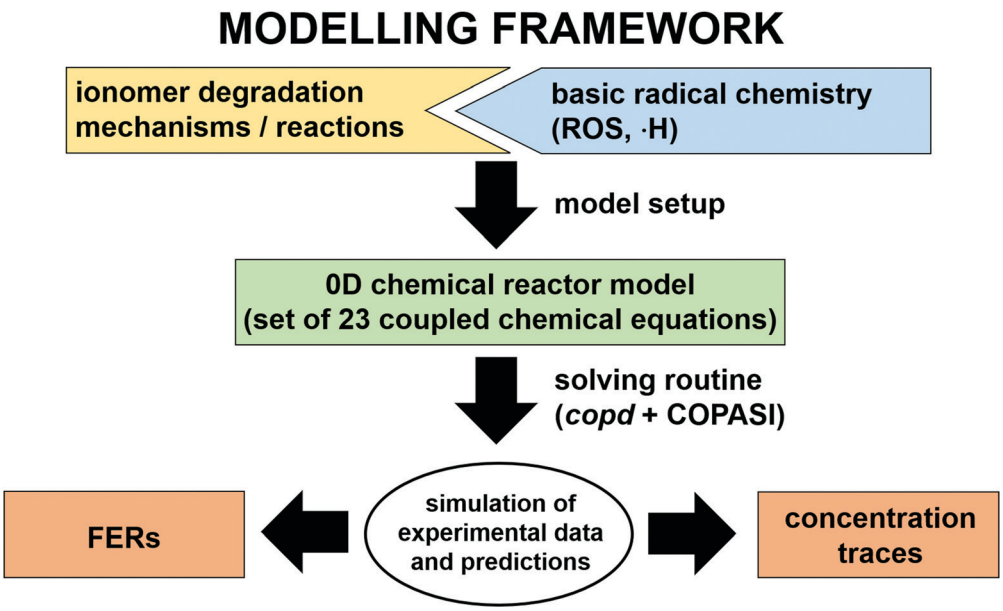

Scheme 5 Schematic drawing of the modelling framework presented in this article. Ionomer degradation mechanisms/reactions[33–35] (see Scheme 6) are combined with basic radical reactions of ROS and $^{\bullet}H$[14–28] to yield a zero-dimensional chemical reactor model comprising a set of coupled chemical equations. This system of differential equations is solved by a combination of the self-developed tool *copd* and freely available software COPASI.[85] Fluoride emission rates and concentration traces (*e.g.* HF, CO_2, ionomer moieties) can be simulated and predicted.

6. For the 0D chemical reactor a constant concentration (steady-state) of H_2O_2 is assumed.

7. A constant total iron concentration $[Fe^{x+}] = [Fe^{2+}] + [Fe^{3+}]$ within the reactor is assumed, unless otherwise stated.

8. Chemical degradation of the membrane generally starts at the side-chain and proceeds (up to seven CF_2 groups) along the backbone (Scheme 6).

9. For R_{15}, R_{16} and $R_{17–23}$ it is assumed that the first step (*i.e.* the attack of the hydroxyl radical) is rate-determining,[20,28,33] which leads to the rate laws given in Table 1.

10. To account for the temperature-dependence of the rate constants, the Arrhenius approach (eqn (10)) is chosen. The necessary kinetic data are summarised in Table 1.

$$k = A e^{-\frac{E_a}{RT}} \quad (10)$$

The rate constants for R_{15} and R_{16} were estimated by Wong and Kjeang,[33] and all other rate constants were obtained experimentally.[14–28] For all ionomer degradation reactions (R_{14}–R_{23}) the same (average) activation energy of 70 kJ mol^{-1} was assumed.[31,86]

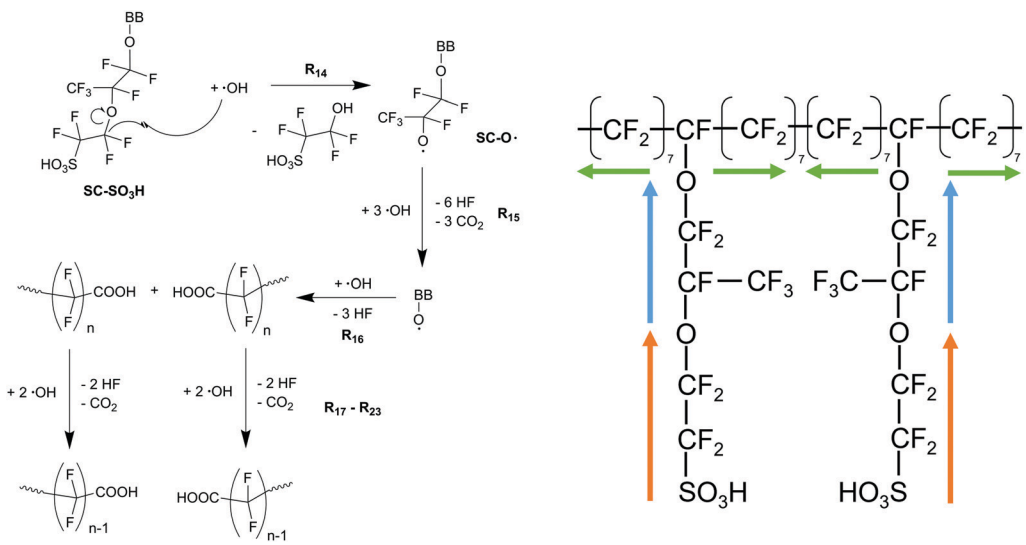

Scheme 6 Left: Side chain degradation mechanism[33–35] used in the following modelling approach. Right: Upon initiation at the side chain (orange and blue arrows), membrane degradation proceeds in both directions along the backbone equally (indicated by green arrows).

Open Access Article. Published on 26 February 2020. Downloaded on 2/15/2026 7:49:42 AM.
This article is licensed under a Creative Commons Attribution-NonCommercial 3.0 Unported Licence.

Table 1 Summary of kinetic data used in this study. For each reaction (R_1–R_{23}), rate constant k at 25 °C (= 298.15 K) in L mol^{-1} s^{-1}, activation energy E_a in kJ mol^{-1} and pre-exponential factor A in L mol^{-1} s^{-1} are given

Reaction			k (T = 298.15 K) [L mol^{-1} s^{-1}]	E_a [kJ mol^{-1}]	A [L mol^{-1} s^{-1}]
R_1	$Fe^{2+} + H_2O_2 + H^+ \rightarrow Fe^{3+} + {}^\bullet OH + H_2O$	$r_1 = k_1[Fe^{2+}][H_2O_2]$	66	35.4^{15}	$1.05 \times 10^{8\,15}$
R_2	$Fe^{3+} + H_2O_2 \rightarrow Fe^{2+} + {}^\bullet OOH + H^+$	$r_2 = k_2[Fe^{3+}][H_2O_2]$	8.6×10^{-4}	126^{22}	$8.43 \times 10^{18\,22}$
R_3	$Fe^{2+} + {}^\bullet OH + H^+ \rightarrow Fe^{3+} + H_2O$	$r_3 = k_3[Fe^{2+}][{}^\bullet OH]$	$3.6 \times 10^{8\,19\,a}$	9^{19}	1.37×10^{10}
R_4	$Fe^{2+} + {}^\bullet OOH + H^+ \rightarrow Fe^{3+} + H_2O_2$	$r_4 = k_4[Fe^{2+}][{}^\bullet OOH]$	$1.2 \times 10^{6\,23}$	42^{23}	2.74×10^{13}
R_5	$Fe^{3+} + {}^\bullet OOH \rightarrow Fe^{2+} + H^+ + O_2$	$r_5 = k_5[Fe^{3+}][{}^\bullet OOH]$	$8.1 \times 10^{4\,18}$	$33^{17,18}$	4.9×10^{10}
R_6	$H_2O_2 \rightarrow 2\,{}^\bullet OH$	$r_6 = k_6[H_2O_2]$	6.5×10^{-23} [s^{-1}]	201^{21}	10^{13} [s^{-1}]^{21}
R_7	$ {}^\bullet OH + H_2O_2 \rightarrow {}^\bullet OOH + H_2O$	$r_7 = k_7[{}^\bullet OH][H_2O_2]$	$3.0 \times 10^{7\,26\,a}$	14^{26}	8.43×10^{9}
R_8	$ {}^\bullet OOH + H_2O_2 \rightarrow {}^\bullet OH + H_2O + O_2$	$r_8 = k_8[{}^\bullet OOH][H_2O_2]$	3.7^{14}	$33.5^{14\,b}$	2.71×10^{6}
R_9	$2\,{}^\bullet OOH \rightarrow H_2O_2 + O_2$	$r_9 = k_9[{}^\bullet OOH]^2$	$9.1 \times 10^{5\,24\,a}$	20.6^{16}	3.70×10^{9}
R_{10}	$2\,{}^\bullet OH \rightarrow H_2O_2$	$r_{10} = k_{10}[{}^\bullet OH]^2$	$5.3 \times 10^{9\,27\,a}$	8^{25}	1.33×10^{11}
R_{11}	$ {}^\bullet OOH + {}^\bullet OH \rightarrow H_2O + O_2$	$r_{11} = k_{11}[{}^\bullet OOH][{}^\bullet OH]$	$1.1 \times 10^{10\,27\,a}$	14.2^{16}	3.39×10^{12}
R_{12}	$ {}^\bullet OH + H_2 \rightarrow H_2O + {}^\bullet H$	$r_{12} = k_{12}[{}^\bullet OH][H_2]$	$3.9 \times 10^{7\,27\,a}$	19.2^{27}	9.14×10^{10}
R_{13}	$ {}^\bullet H + O_2 \rightarrow {}^\bullet OOH$	$r_{13} = k_{13}[{}^\bullet H][O_2]$	$2.2 \times 10^{10\,27\,a}$	10.3^{16}	1.37×10^{12}
R_{14}	$SC–SO_3H + {}^\bullet OH \rightarrow SC–O^\bullet + HOCF_2CF_2SO_3H$	$r_{14} = k_{14}[SC–SO_3H][{}^\bullet OH]$	$3.7 \times 10^{6\,20}$	70^{c}	6.80×10^{18}
R_{15}	$SC–O^\bullet + 3\,{}^\bullet OH \rightarrow BB–O^\bullet + 6HF + 3CO_2$	$r_{15} = k_{15}[SC–O^\bullet][{}^\bullet OH]$	$3 \times 10^{7\,33}$	70^{c}	5.51×10^{19}
R_{16}	$BB–O^\bullet + {}^\bullet OH \rightarrow 2–(CF_2)_nCOOH + 3HF$	$r_{16} = k_{16}[BB–O^\bullet][{}^\bullet OH]$	$8.5 \times 10^{7\,33}$	70^{c}	1.56×10^{20}
R_{17}–R_{23} ($7 \leq n \leq 1$)	$–(CF_2)_nCOOH + 2\,{}^\bullet OH \rightarrow –(CF_2)_{n-1}COOH + CO_2 + 2HF$	$r_{un} = k_{un}[–(CF_2)_nCOOH][{}^\bullet OH]$	$1.0 \times 10^{6\,28\,d}$	70^{c}	1.84×10^{18}

[a] Rate constants were recalculated for T = 298.15 K. [b] Activation energy is estimated between 6 and 10 kcal mol^{-1}. [c] Average activation energy found in various degradation experiments.[31,86] [d] Upper limit for the attack of ${}^\bullet OH$ on CF_3COOH.[28]

Although not many experimental activation parameters have been established, the use of DFT-calculated Arrhenius parameters is problematic because due to the subtle interplay of solvent and counter-ion effects they may substantially deviate from their experimental counterparts.[84,87] The set of coupled chemical reactions shown in Table 1 gives rise to a system of coupled differential equations (displayed in Table 2), which needs to be solved in order to obtain the time traces of all participating chemical species. An overview of parameters (concentrations, temperature, thickness of the membrane)

Table 2 System of coupled differential equations for all relevant species

Species	Differential equation
$[Fe^{2+}]$	$\frac{d[Fe^{2+}]}{dt} = -r_1 + r_2 - r_3 - r_4 + r_5$
$[Fe^{3+}]$	$\frac{d[Fe^{3+}]}{dt} = -\frac{d[Fe^{2+}]}{dt} = r_1 - r_2 + r_3 + r_4 - r_5$
$[{}^\bullet H]$	$\frac{d[{}^\bullet H]}{dt} = r_{12} - r_{13}$
$[{}^\bullet OOH]$	$\frac{d[{}^\bullet OOH]}{dt} = r_2 - r_4 - r_5 + r_7 - r_8 - 2r_9 - r_{11} + r_{13}$
$[{}^\bullet OH]^b$	$\frac{d[{}^\bullet OH]}{dt} = r_1 - r_3 + 2r_6 - r_7 + r_8 - 2r_{10} - r_{11} - r_{12} - r_{14} - 3r_{15} - r_{16} - 2(r_{17} + r_{18} + r_{19} + r_{20} + r_{21} + r_{22} + r_{23})$
$[HF]^b$	$\frac{d[HF]}{dt} = 6r_{15} + 3r_{16} + 2(r_{17} + r_{18} + r_{19} + r_{20} + r_{21} + r_{22} + r_{23})$
$[CO_2]^b$	$\frac{d[CO_2]}{dt} = 3r_{15} + r_{17} + r_{18} + r_{19} + r_{20} + r_{21} + r_{22} + r_{23}$
$[SC–SO_3H]$	$\frac{d[SC - SO_3H]}{dt} = -r_{14}$
$[SC–O^\bullet]$	$\frac{d[SC–O^\bullet]}{dt} = r_{14} - r_{15}$
$[BB–O^\bullet]$	$\frac{d[BB–O^\bullet]}{dt} = r_{15} - r_{16}$
$[HOCF_2CF_2SO_3H]$	$\frac{d[HOCF_2CF_2SO_3H]}{dt} = r_{14}$
$[–(CF_2)_nCOOH]^{a,b}$	$\frac{d[–(CF_2)_nCOOH]}{dt} = 2r_{16} - r_{17}$
$[–(CF_2)_{n-1}COOH]^{a,b}$	$\frac{d[–(CF_2)_{n-1}COOH]}{dt} = r_{17} - r_{18}$

[a] n = 7. [b] For the rate constants the following relation is valid: $k_{un} = k_m$ for $17 \leq m \leq 23$.

 This journal is © the Owner Societies 2020

Open Access Article. Published on 26 February 2020. Downloaded on 2/15/2026 7:49:42 AM.
This article is licensed under a Creative Commons Attribution-NonCommercial 3.0 Unported Licence.

Table 3 Overview of parameters and their typical ranges used in the simulations of *in situ* conditions

Parameter	Values
$[H_2O_2]$	0.1–10 mM (constant)
$[Fe^{2+}]_0$	1–100 ppm[a]
$[Fe^{3+}]_0$	1–100 ppm[a]
$[Fe^{x+}]$	$= [Fe^{2+}]_0 + [Fe^{3+}]_0$ (constant)
$[SC\text{–}SO_3H]_0$	1.81 M[34 b]
$[H_2]$	10 mM (constant)[31]
$[O_2]$	7.5 mM (constant)[31]
T	333.15–368.15 K
$\delta_{membrane}$	25–50 μm

[a] 1 ppm Fe corresponds to 1.79×10^{-5} M. [b] $[SC\text{–}SO_3H]_0$ is calculated as the ratio between dry membrane density $\rho_{membrane}$ and BOL equivalent weight EW_0.[34]

which are used in the model and can be adjusted freely is presented in Table 3.

Methods

The system of coupled differential equations was solved by using a combination of the freely available kinetic simulation software COPASI[85] (http://copasi.org) and an automatisation routine (COPASI driver, developed by us) implemented in the programming language Perl. All inputs are provided in a plain text file (obeying a certain syntax) and are then interpreted by the routine which generates the inputs for the commandline version of COPASI (version 4.24 (Build 197)). The results are processed by *copd* to yield output text files and graphical representations (time traces and rate plots; generated *via gnuplot* (version 5.2 patchlevel 4)), which allow a first fast assessment of the received data. Examples of an input file and output files of the routine are provided in the ESI.† Origin Pro 8 was used to fit the calculated data shown in Fig. 13. Simulations are generally fast (4.4 s for 100 h real-time simulation of a chemical reactor on a Windows 10 64-bit PC equipped with an Intel® Core i5-3210M processor and 8GB RAM). The kinetic framework can also be used with Linux. A web interface of the routine can be freely accessed under http://ptc-pc-139.tugraz.at/cgi-bin/Membrane_Degradation/.

To inspect if the results generated by the *COPASI driver* are of general nature, we have also implemented the equations in Mathematica (Version 11). A comparison of the results obtained from both the *copd* routine and the Mathematica implementation is shown in the ESI.† The used Mathematica code is available in the ESI† and free to use.

Results and discussion

To establish a holistic chemical degradation modelling framework based on the equations presented in Table 1, several aspects – the interplay of iron species and radicals, their influence on the ionomer degradation and the dependence of fluoride emission on the temperature, $[Fe^{x+}]$ and $[H_2O_2]$ – are highlighted in this section. Furthermore, the model allows analysing the entire cause and effect chain of chemical degradation phenomena ranging from basic radical formation reactions to the (measurable) manifestations of membrane degradation (fluoride emissions, loss of ionomer moieties and loss of ion exchange capacity).

Dynamic equilibrium between ferrous and ferric ion

Transition metals like Cu^+ or Co^{2+} are also capable of converting H_2O_2 to ROS. The modular setup of the framework allows that reactions for additional metal contaminants can be added to the system easily. Iron ions, however, are known as contaminants in fuel cell membranes.[57,60–62] We consider iron as a paradigm of all ''Fenton-active'' metal salts, whose exact distribution and concentrations remain unresolved. Furthermore, the reactions of Fe^{2+} and Fe^{3+} with H_2O_2 and radical species are very well studied (see R_1–R_5).[15,17–19,22,23,58,59,88,89] All 5 reactions can be characterised as redox reactions and constitute a recycling system for the oxidation state of the iron. As a dynamic equilibrium between the two main oxidation states of iron (+II and +III) is established, it should not be relevant in which oxidation state the iron ions are present at the initial state of the simulation.

This hypothesis was tested by comparing the time traces for the iron and radical species for two test cases – in the first one

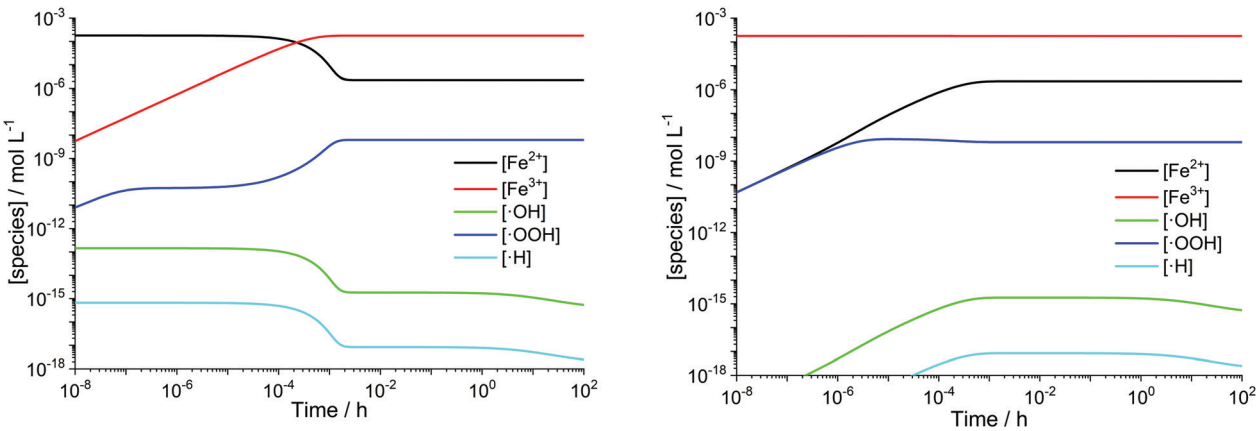

Fig. 3 log–log plots of $[Fe^{x+}]$ and radical concentrations as a function of time for T = 363.15 K. Left: $[H_2O_2]$ = 1 mM, $[Fe^{2+}]_0$ = 10 ppm. Right: $[H_2O_2]$ = 1 mM, $[Fe^{3+}]_0$ = 10 ppm.

Open Access Article. Published on 26 February 2020. Downloaded on 2/15/2026 7:49:42 AM.
This article is licensed under a Creative Commons Attribution-NonCommercial 3.0 Unported Licence.

10 ppm Fe is present in +II state at $t = 0$ and in the second one the same amount of Fe is in the +III state at $t = 0$. The results are presented in Fig. 3 and indicate that in the first few seconds of the simulation a constant ratio between both iron species is formed. From this moment on 99% of the iron species are in the +III state and lead to matching concentration curves for all depicted chemical species for both cases. The graphical representation of the time traces for the chemical reactor with $[Fe^{2+}] = 10$ ppm and $[Fe^{3+}] = 0$ ppm (left side of Fig. 3) reveals a remarkable correlation between the concentrations of the ferrous ion and the radicals $^{\bullet}$OH and $^{\bullet}$H. The time traces representing these radicals are strongly influenced by the transient concentration of ferrous ions. [$^{\bullet}$OH] and [$^{\bullet}$H] drop as soon as major parts of the ferrous ion are oxidised. This observation is reasonable, as the Fenton reaction (R_1) is one of the prominent sources of $^{\bullet}$OH. The concentration of $^{\bullet}$H follows the time trace of $^{\bullet}$OH, as their sole source is the reaction between H_2 and $^{\bullet}$OH (R_{12}). Parallel to the oxidation of iron, the concentration of $^{\bullet}$OOH increases (with a short stagnation) until reaching a steady-state concentration after a few seconds.

A similar behaviour is observable for the inverse case – all iron ions are in +III at $t = 0$ – shown on the right side of Fig. 3. The reduction of ferric ions to ferrous ions is only carried out *via* the reaction with H_2O_2 (R_2) and subsequently with newly formed $^{\bullet}$OOH (R_5). Up to 10^{-6} s, the concentrations of Fe^{2+} and $^{\bullet}$OOH, which are both products of R_2, are the same and afterwards, the participation of the species in other chemical reactions leads to a bifurcation of the curves. The concentration of Fe^{3+} is only weakly influenced, as just about 1% of the ferric ions are reduced to ferrous ions. This finding is in good agreement with the results from the quasi-steady-state approach by Gubler *et al.*,[31] who found that in the steady-state >99% of the iron ions are Fe^{3+}.

The obtained range of the radical concentrations for the time between 10^{-3} h and 100 h are in accordance with the results by Gubler *et al.*,[31] who calculated [$^{\bullet}$OOH] $\approx 10^{-10}$ M, [$^{\bullet}$OH] $\approx 10^{-16}$ M and [$^{\bullet}$H] $\approx 10^{-19}$ M. Discrepancies might be explained by the fact that the model presented here does not rely on a steady-state approach and additionally, the temperature dependence of the chemical reactions is included.

Time evolution of membrane degradation

The time-scale at which a steady-state of the iron and radical species (except for $^{\bullet}$OH and $^{\bullet}$H) is established is clearly separated from that of the evolution of the membrane degradation products. As shown in Fig. 3 iron and radical species reach their final concentrations after a few seconds (and then do not depend on differences in the initial concentrations of Fe^{2+} and Fe^{3+} anymore). The evolution of the ionomer moieties and degradation products (HF and CO_2) happens on a much longer time-scale as shown in Fig. 4. The radical ether cleavage at the side chain (first step in the degradation mechanism) leads to a decrease in sulfonic acid head group concentration (see Scheme 6). Immediately after the start of degradation the product of the radical ether cleavage SC–O$^{\bullet}$ is built up and, with a certain delay, also BB–O$^{\bullet}$ and the carboxylic acid terminated main chain fragments are generated. The occurrence of the intermediates also correlates with the drop of concentration of $^{\bullet}$OH observed after a few hours (see Fig. 3), as the degradation of these intermediates (R_{15}–R_{23}) consumes additional $^{\bullet}$OH. Despite the favourable kinetics for the attack of the membrane by $^{\bullet}$OH with rate constants $>10^6$ L mol^{-1} s^{-1} membrane degradation is greatly decelerated by the low steady-state concentration of $^{\bullet}$OH (see Fig. 3).

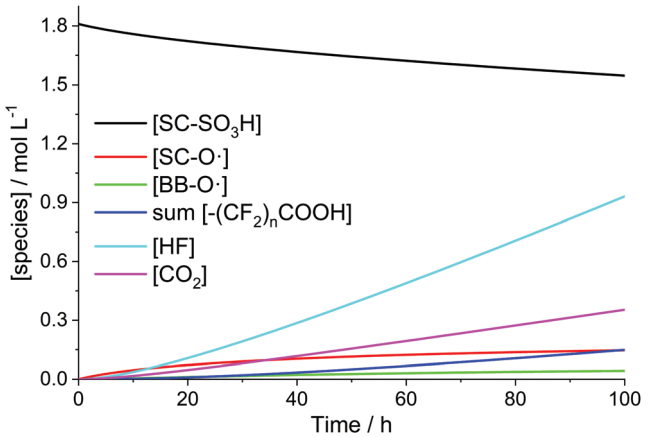

Fig. 4 Time traces of PFSA ionomer functional groups and degradation products for $[H_2O_2] = 1$ mM, $[Fe^{2+}]_0 = 10$ ppm and $T = 363.15$ K.

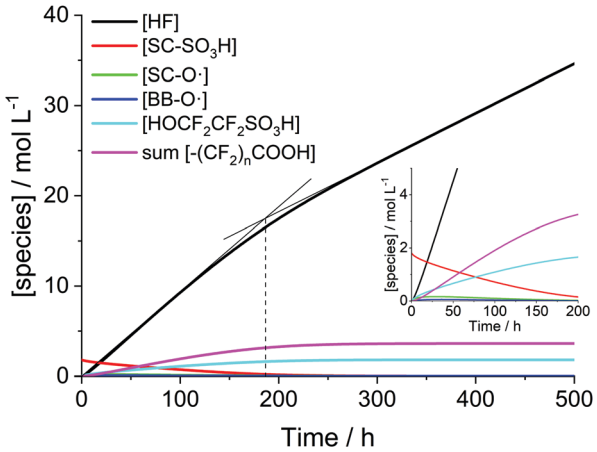

Fig. 5 Time traces of PFSA ionomer functional groups and degradation products for $[H_2O_2] = 5$ mM, $[Fe^{2+}]_0 = 10$ ppm and $T = 368.15$ K. The bend in the concentration trace of HF (change in the degradation mechanism) is indicated by two intersecting lines and a dashed line.

When plotting the concentration traces for harsher conditions ($[H_2O_2] = 5$ mM, $[Fe^{2+}]_0 = 10$ ppm and $T = 368.15$ K; Fig. 5), the curve for HF levels off in the area around 200 h. Up to this point, the fast degradation reactions of the side chain (R_{15} and R_{16}) mainly contribute to the fluoride emission. As soon as most of the side chain is consumed (at around 200 h), the emitted fluoride stems exclusively from the unzipping of the main chain (R_{17-23}), which is characterized by a smaller rate constant and becomes rate-determining in terms of fluoride emission.

This journal is © the Owner Societies 2020

Open Access Article. Published on 26 February 2020. Downloaded on 2/15/2026 7:49:42 AM.
This article is licensed under a Creative Commons Attribution-NonCommercial 3.0 Unported Licence.

Trends in fluoride emission rates

Among the most important parameters to assess the state of health of an ionomer membrane is the fluoride emission rate, which is usually determined in effluent water by using fluoride sensitive electrodes or high performance liquid chromatography.[5] The FER is inversely proportional to the life-time of the membrane as it is directly linked to its loss of mass, which will be highlighted further below in the text.

Besides time traces for the concentrations of the chemical species, the *copd* routine outputs FER data derived from the concentration of HF. The FER values (averaged over 100 h) were calculated for different $[Fe^{2+}]_0$ and $[H_2O_2]$ values and T = 70 °C (see Fig. 6). For low $[Fe^{2+}]_0$ and $[H_2O_2]$, small FER values are obtained, as expected. The FER shows a strong dependency on both $[Fe^{2+}]_0$ and $[H_2O_2]$ which is indicated by the orange and black lines. Hence, a low concentration of both iron contaminants and detrimental hydrogen peroxide is necessary to protect the chemical integrity of the membrane.

Another factor which greatly influences the fluoride emission is the temperature within the fuel cell membrane (see Fig. 7). By increasing the temperature by only 10 K (*e.g.* going from 333.15 K to 343.15 K) while keeping $[Fe^{2+}]$ constant, a gain in the fluoride emission rate of up to one order of magnitude results. The increase in fluoride emission is less pronounced for higher initial concentrations of Fe^{2+}.

In addition to the FER, the ion exchange capacity of the ionomer is also an indicator of the chemical integrity of the membrane. When the sulfonic acid moieties are eliminated due to degradation phenomena, the ion exchange capacity (IEC) decreases. To investigate the correlation with the fluoride emission rate, we calculated the IEC (at BOL) as the ratio of the amount of sulfonic acid groups in mmol (n_0) and the dry mass of the ionomer in g ($m_{dry,0}$) in the following equation:[33]

$$IEC_0 = \frac{n_0(SO_3H)}{m_{dry,0}} \quad (11)$$

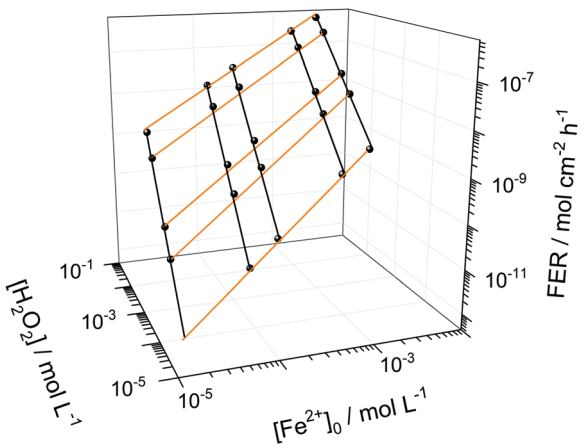

Fig. 6 Logarithmic depiction of the fluoride emission rate (averaged over 100 h) as a function of hydrogen peroxide concentration and initial ferrous ion concentration for T = 343.15 K and $\delta_{membrane}$ = 50 μm. The black lines indicate constant initial ferrous ion concentration and the orange lines indicate constant hydrogen peroxide concentration.

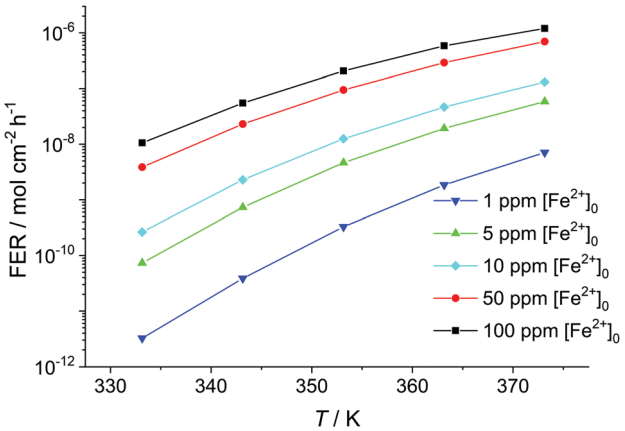

Fig. 7 Fluoride emission rate (averaged over 100 h) given in mol cm^{-2} h^{-1} calculated as a function of temperature in K for $[H_2O_2]$ = 1 mM and $\delta_{membrane}$ = 50 μm.

When the ionomer is subjected to chemical degradation, the number of sulfonic acid group decreases, and the mass of the ionomer is diminished by the loss of CF_2 groups ($m_C + m_F$) and the fragment $HOCF_2CF_2SO_3H$ ($m_{fragment}$) formed in R_{14}:

$$IEC = \frac{n(SO_3H)}{m_{dry,0} - m_C - m_F - m_{fragment}} \quad (12)$$

For the calculations of the IEC after a simulated degradation test, a membrane area of 25 cm^2, a constant membrane thickness of 50 μm and hence a volume of 1.25 × 10^{-4} L are assumed. The density of Nafion is 1.98 g cm^{-3}.[90] The FER values (averaged over 100 h) are plotted as a function of IEC values obtained at the end of simulation (100 h) in Fig. 8. With increasing temperature and iron contaminant concentration the FER is increased and approaches a value of about 10^{-6} mol cm^{-2} h^{-1}. At the same time, the IEC drops until reaching 0 mmol g^{-1}, the point at which all side chains are degraded (left side of Fig. 8). In the other direction, it is evident that a value of 0.91 mmol g^{-1} is approached, which corresponds to the IEC_0 value of a pristine membrane,[13]

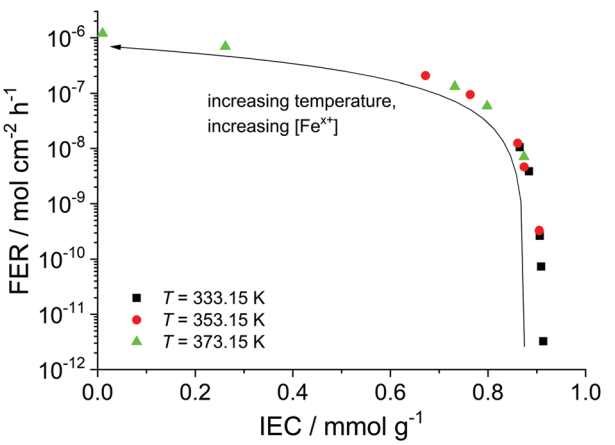

Fig. 8 Fluoride emission rate (averaged over 100 h) is plotted as a function of the ion exchange capacity (at t = 100 h). The arrow indicates increasing temperature and iron concentration.

Open Access Article. Published on 26 February 2020. Downloaded on 2/15/2026 7:49:42 AM.
This article is licensed under a Creative Commons Attribution-NonCommercial 3.0 Unported Licence.

as virtually no side chains are consumed at lower temperatures (333.15 K) and lower iron concentrations (1 ppm). The IEC is only affected critically, when the FER exceeds a certain threshold (about 10^{-7} mol cm^{-2} h^{-1}).

Influence of iron input and leaching on membrane degradation

For the results presented so far, the total iron concentration [Fe^{x+}] was kept constant over the whole course of the simulation. The implications of changing the total iron concentration due to input of additional iron (*e.g.* demetallation of the Fe–N–C catalyst;[38,39] originating from stainless steel end plates[57,60]) or loss of iron are demonstrated in the following paragraphs.

For the analysis, it was assumed that all iron, which is added or lost, is in the oxidation state +II. This assumption is justified, as simulations presented above show that the dynamic equilibrium between both oxidation states of iron is established within seconds. The rate constant, which describes the input or loss (output) of iron ($k_{I/O}$), was calculated so that the final total iron concentrations are reached at the end of the simulation (linear increase and decrease). This means that $k_{I/O} = \pm 4.972 \times 10^{-10}$ mol L^{-1} s^{-1} (positive for 10 → 20 ppm and negative for 10 → 0 ppm) is obtained. The differential equation for [Fe^{2+}] can be written as

$$\frac{d[Fe^{2+}]}{dt} = -r_1 + r_2 - r_3 - r_4 + r_5 + k_{I/O} \qquad (13)$$

The results, which are depicted in Fig. 9, reveal that the input or leaching of Fe^{x+} has a great influence on the kinetics of the degradation, as expected. The green curves show the cases when [Fe^{x+}] is decreased from 10 to 0 ppm. At the end of the simulation the slope of the green curves tends to 0, as the system becomes almost depleted of [Fe^{x+}]. For the increase of [Fe^{x+}] from 10 to 20 ppm (blue curves) the slope of the curves grows until the blue curves are parallel to the black curves (20 ppm [Fe^{x+}]). To avoid the acceleration of chemical degradation, it is highly important to optimize the constituents of the fuel cell (*e.g.* the end plates or the Fe–N–C catalysts) in a way that the input of additional iron species is minimized.

Comparison with experimental data

The simulation results presented so far were derived from a model that assumes a 0D chemical reactor. In reality, membrane degradation is a complex interplay of chemical and physical (thermal and mechanical) processes. To demonstrate that our model, despite its limitations, produces reasonable results, we will compare simulation results with a number of experimental data sets in the following paragraphs.

Wong and Kjeang[33] validated their membrane degradation model by comparing it to the results from a cyclic open circuit voltage accelerated stress test (COCV AST). ^{19}F NMR spectroscopy was employed to monitor the loss of functional groups (–SO_3H, CF(s), CF(m); for assignment see Fig. 2) during the AST. The measured concentrations of these groups after 0, 20, 50 and 70 h are shown in Fig. 10. Based on the experimental parameters ([Fe^{x+}] = 6 ppm) the results were reproduced by the

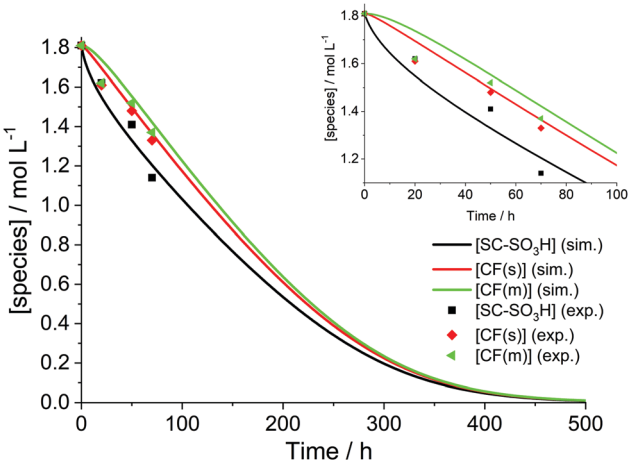

Fig. 10 Temporal evolution of the ionomer functional moieties. The inset shows the curves and the experimental data during the first 100 h. Simulation (sim.) parameters: T = 368.15 K, [H_2O_2] = 5.2 mM, [Fe^{2+}]$_0$ = 6 ppm. Experimental (exp.) results were taken from an AST ([Fe^{x+}] = 6 ppm) by Wong and Kjeang.[33]

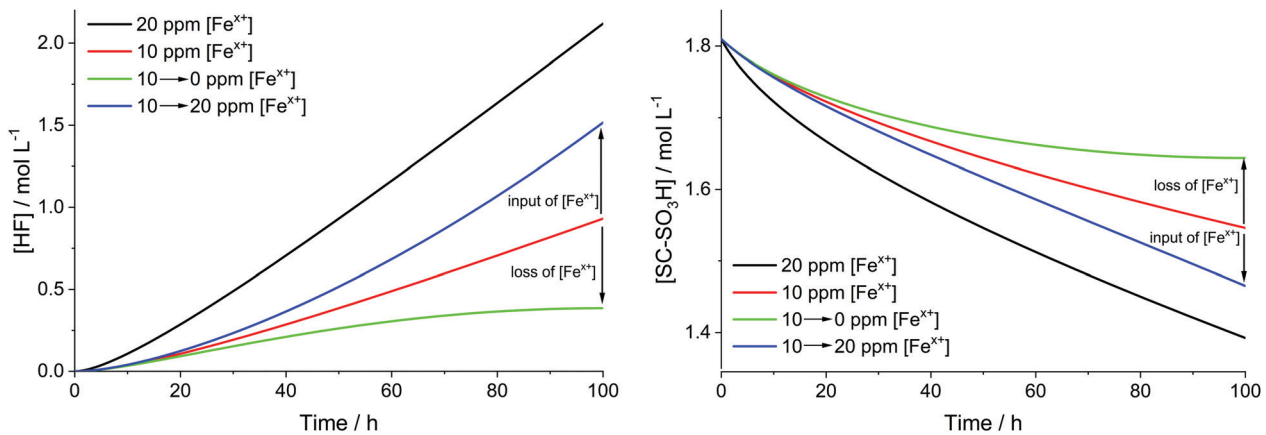

Fig. 9 Influence of total iron concentration [Fe^{x+}] on the time traces of HF (left) and SC–SO_3H (right) for T = 363.15 K and [H_2O_2] = 1 mM. The green and blue curves indicate cases where additional iron is added to the system (10 → 20 ppm, blue) and removed from the system (10 → 0 ppm, green).

This journal is © the Owner Societies 2020

Open Access Article. Published on 26 February 2020. Downloaded on 2/15/2026 7:49:42 AM.
This article is licensed under a Creative Commons Attribution-NonCommercial 3.0 Unported Licence.

Table 4 Error estimations based on experimental data (^{19}F NMR)[12,13] compared to the deviations between experimental and simulated values (for 20, 50 and 70 h) shown in Fig. 10

	Relative deviations between experimental (c_{exp}) and simulated concentrations (c_{sim})[a]			Experimental errors[b]	
PFSA moiety	20 h	50 h	70 h	Lowest	Highest
–CF_2SO_3H (≙SC–SO_3H)	5%	6%	6%	±2%	±3%
CF(s)	6%	2%	3%	±7%	±9%
CF(m)	8%	3%	4%	±8%	±10%

[a] Calculated as $\frac{|c_{exp} - c_{sim}|}{c_{exp}} \times 100\%$. [b] Determined from the error bars of the experimental results.

simulation. The concentrations of the tertiary carbon moieties in Fig. 10 were calculated using the following relations:[33]

$$[CF(s)] = [SC–SO_3H] + [SC–O^\bullet] \quad (14)$$

$$[CF(m)] = [SC–SO_3H] + [SC–O^\bullet] + [BB–O^\bullet] \quad (15)$$

Since $[H_2O_2]$ and the exact temperature at which the test was run were not stated[33,91] (OCV phase under high temperature/low RH (relative humidity) conditions as described by Lim *et al.*[91]), these parameters were adjusted in the simulation to give the best agreement between the experimental data and the simulation. $[H_2O_2]$ was set to 5.2 mM and the temperature to 368.15 K to yield the time traces in Fig. 10. The temperature (95 °C) is reasonable, as compatible temperatures are employed in fuel cell tests to accelerate degradation.[37,92] The values of $[H_2O_2]$ used in the simulations will be discussed below. Under these conditions, a complete consumption of ionomer moieties (SC–SO_3H, CF(s) and CF(m)) is accomplished within approx. 500 hours. From this moment on only –COOH terminated main chain fragments are present in the chemical reactor.

As no error bars were presented with the experimental data[33] used in Fig. 10, errors were estimated based on similar ^{19}F NMR data.[12,13] The results, which are outlined in Table 4, indicate that the relative deviations for both CF(s) and CF(m) are below or the same as the lowest experimental errors. For SC–SO_3H the experimental errors are about half the size of the relative deviations between experimental and simulated data in Fig. 10. These findings might also provide an explanation for the similarity of the concentration values for all three monitored groups at 20 h in Fig. 10. Upon consideration of the experimental errors shown in Table 4 a similar trend in concentration (as for 50 and 70 h) is expected.

Not only the loss of ionomer moieties during *in situ* tests but also the temporal evolution of the FER during such experiments can be simulated. The red dots in Fig. 11 show the experimental FER values obtained in a 10 h long OCV hold experiment by Singh *et al.*[35] The data could be well reproduced (black line) by the kinetic framework ($[H_2O_2]$ = 4 mM, $[Fe^{2+}]_0$ = 10 ppm, $\delta_{membrane}$ = 50 µm). Due to the lack of diffusion in the 0D chemical reactor model a differentiation between fluoride emission on the cathode and anode side is not possible. Therefore, the sum of the experimental FER values, which were higher for the cathode side, had to be used for comparison.

Recently, Futter *et al.*[36] obtained FER values in the range of 10^{-7} to 6×10^{-7} mol cm^{-2} h^{-1} depending on the conditions of

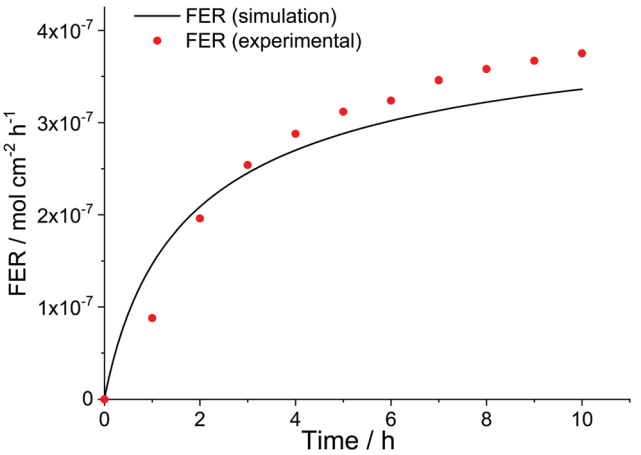

Fig. 11 Time evolution of fluoride emission rate during an OCV hold test. Simulation parameters: T = 368.15 K, $[H_2O_2]$ = 4 mM, $[Fe^{2+}]_0$ = 10 ppm; $\delta_{membrane}$ = 50 µm. Experimental results (sum of fluoride emission rate for both anode and cathode side) were taken from an OCV hold test (T = 368.15 K) by Singh *et al.*[35]

the performed ASTs (p_{anode} = 1.5–2.5 bar, $p_{cathode}$ = 1.5–2.3 bar, RH = 30–75%). To compare the experimental results with the model, the authors multiplied the experimentally obtained FER values by a factor of 20.8 to account for non-detectable fluorine (in the form of membrane fragments). Thus, the FER values for detectable fluorine were found to be between 5×10^{-9} and 3×10^{-8} mol cm^{-2} h^{-1}.[36] As our model only calculates the FER based on detectable fluorine, the modelling result will be compared with these values. When taking the conditions from the stress test and the model[36] ($[Fe^{x+}]$ = 2.5 ppm; $[Fe^{2+}]_0/[Fe^{3+}]_0$ = 1; T = 368.15 K, Nafion® XL membrane ($\delta_{membrane}$ = 25 µm) with a 8.33 µm thick reinforcement layer) and setting $[H_2O_2]$ from 0.5 to 3 mM, FER values ranging from 3×10^{-9} to 3×10^{-8} mol cm^{-2} h^{-1} (averaged over 100 h) were obtained from the simulation. In addition to the reinforcement layer, cerium ions are incorporated into the membrane to protect the ionomer from ROS-mediated degradation. The role of cerium ions as scavengers will be discussed in more detail at the end of the Results section.

These examples demonstrate that predictions for the concentration of ionomer functional groups and the FER with reasonable assumptions are possible for *in situ* conditions. For the first two examples (shown in Fig. 10 and 11) the assumed values for $[H_2O_2]$ are higher compared to experimental[52,53] and

Open Access Article. Published on 26 February 2020. Downloaded on 2/15/2026 7:49:42 AM.
This article is licensed under a Creative Commons Attribution-NonCommercial 3.0 Unported Licence.

Table 5 Experimental conditions used in the Fenton test[37]

Parameter	Values
T	80 °C = 353.15 K
$A_{membrane}$	*ca.* 25 cm^2
$\delta_{membrane}$	50 μm
$[H_2O_2]_0$	3 wt% = 0.98 M
$[Fe_{2+}]_0$	13 ppm (impregnated into the membrane)
Duration of test	96 h

simulated data.[30,31] For the last example discussed in the paragraph above, the cerium scavengers incorporated into the membrane lead to a decreased FER; hence the FER value without any cerium additives is estimated to be 10^{-7} to 10^{-5} mol cm^{-2} h^{-1} (2 orders of magnitude higher, see below for discussion). This means that the parameters $[H_2O_2]$ and $[Fe^{x+}]$ have to be set to a higher value to reproduce the fluoride emission rates obtained by Futter *et al.*[36]

It should, however, be kept in mind that the 0D reactor can neither account for additional formation mechanisms of radical species (*e.g.* at Pt surfaces[73–75]) and additional membrane degradation mechanisms (such as the $^{\bullet}H$ mediated membrane degradation[13]) nor for potential-dependent redox recycling of iron species.[34] Furthermore, the experimental $[H_2O_2]$ values (micromolar range) were obtained under OCV conditions and a temperature of 60 °C,[52,53] whereas the simulations were performed at 95 °C. The situation is aggravated by the fact that under low humidity conditions the concentrations of H_2O_2 and contaminants are higher, as the membrane contains less water. All these effects contribute to the membrane degradation and hence a $[H_2O_2]$ lower than that used in the simulation might be sufficient to cause the same effects. In this case the $[H_2O_2]$ used in the simulation can be regarded as an "effective" concentration to trigger the analogue behaviour in the 0D chemical reactor model. When implementing the input of additional iron species, which are migrating from other parts of the PEMFC into the membrane (as shown in Fig. 9), $[H_2O_2]$ can be set to a lower value to obtain the same FER values.

Simulation of Fenton experiments

To demonstrate the versatility of the kinetic framework, *ex situ* conditions in a Fenton test (*i.e.* high $[H_2O_2]$ and (optionally) high $[Fe^{2+}]_0$) were also simulated. In contrast to the fuel cell conditions, in a typical Fenton test a membrane is dipped into a mixture of H_2O_2 and Fe^{2+} salts. Once H_2O_2 is consumed completely, the formation of reactive oxygen species, and hence the membrane degradation process, is paused. Sethuraman *et al.*[37] measured the fluoride emission for a Nafion® 112 ionomer membrane impregnated with Fe^{2+} ions (13 ppm) and submerged into a 3% hydrogen peroxide solution. Further experimental details are summarised in Table 5.

For the simulation (Fig. 12) it was assumed that the total iron concentration stays constant within the membrane (no leaching out of Fe^{x+}). The only species which are washed out of the membrane are the side chain fragment formed in R_{14} and HF. The replacement of the H_2O_2 solution every 24 hours made it necessary to divide the whole process into 4 0D chemical

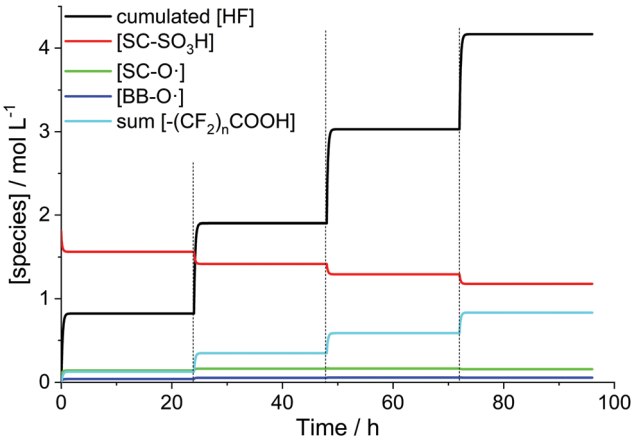

Fig. 12 Simulated time evolution of the concentrations of hydrogen fluoride and ionomer moieties for a Nafion® 112 membrane (impregnated with 13 ppm Fe^{2+}) submerged into a 3% H_2O_2 solution at 80 °C.[37] The dashed lines mark the replacements of the H_2O_2 solution.

reactors. The final concentrations of the chemical species obtained from one chemical reactor serve as initial concentrations for the subsequent chemical reactor. In the case of HF, the concentration values were accumulated. It is clearly visible in Fig. 12 that upon exchange of the H_2O_2 solution the degradation reactions resume. They are stopped again when H_2O_2 is consumed completely, which is accomplished within 2 hours after the replacement. However, it should be kept in mind that the simulations are geared toward *in situ* situations, where all species are contained within the hydrophilic domains of the membrane. In contrast, Fenton tests are characterised by a phase boundary between the ionomer membrane and the solution, in which the membrane is immersed. This comparison was done anyway as, under the assumption that there is no leaching of iron species, the Fenton reaction is confined to the ionomer and does not take place outside the membrane. In addition, H_2O_2 has to diffuse from the solution into the membrane to initiate the Fenton reaction. For a water swollen Nafion® membrane the time for H_2O_2 to diffuse through the whole ionomer membrane (50 μm) is calculated to be 9 s.[31] This value is considerably lower than the time needed for the total consumption of H_2O_2 in the model (*ca.* 2 h); however this might have implications for the concentration within the membrane. In the 0D model a possible concentration gradient between the membrane and the solution is not considered.

Despite the caveats stated in the paragraph above, an average fluoride emission rate of 2.2×10^{-7} mol cm^{-2} h^{-1} could be obtained from the final hydrogen fluoride concentration (4.17 M). This value is in the same order of magnitude as 4×10^{-7} mol cm^{-2} h^{-1} determined by experiment.[31,37]

Membrane lifetime and fluoride emission rate

The side chain degradation mechanism employed in the kinetic framework leads to gradual loss of the side chain altering the properties of the hydrophilic domain. At first, the mechanical stability is not influenced by the degradation process, as only the head group and the first ether bridge are

 This journal is © the Owner Societies 2020

Open Access Article. Published on 26 February 2020. Downloaded on 2/15/2026 7:49:42 AM.
This article is licensed under a Creative Commons Attribution-NonCommercial 3.0 Unported Licence.

lost. Subsequently, R_{16} leads to a fragmentation of the main chain at the anchor position followed by shortening of the main chain (R_{17-23}). From this point on, the mechanical properties of the membrane are affected.

As stated in the introduction, this paper focuses only on the chemical membrane degradation phenomena, neglecting the mechanically and thermally induced destruction of the ionomer. Hence, their contributions to the lifetime of the membrane cannot be evaluated; however an estimation solely based on the results given by the kinetic framework is possible.

The question which still needs to be answered is how to define a criterion for the membrane lifetime. In principle, the FER as an indicator of the state of health of the membrane could serve as this criterion, although it will be more illustrative if a lifetime given in hours is obtained.

As the time traces of the functional moieties of the ionomer can be easily obtained by the *copd* routine, the lifetime could be, in principle, defined based on the concentration of a decisive functional group. The most important functional moiety in the ionomer is, without doubt, the sulfonic acid head group being responsible for the conduction of H^+. Singh *et al.*[35] observed in a COCV AST experiment that a loss of 15.6% of all sulfonic acid groups did not lead to a diminished proton conductivity. At the same time, the membrane was subjected to thinning (decrease of thickness by 1.4%). Lim *et al.*[91] suggested that the decrease of [SC–SO_3H] could be compensated by membrane thinning. Moreover, it was also argued that a fraction of the membrane fragments with intact sulfonic acid groups could reside within the membrane sustaining its conductivity.[35]

Based on these considerations, we define the parameter t_{99} as the time span, which is necessary to degrade 99% of all sulfonic acid groups (*i.e.* almost completion of reaction R_{14}; due to the kinetics of the degradation reactions a degradation of 100% is not possible). Since R_{15} and R_{16} feature higher rate constants, all side chains are removed immediately once R_{14} is completed and only main chain fragments are left.

For different conditions[33,35,36] the t_{99} values and the associated FER (averaged over 100 h) are given in Table 6. It is evident that the higher the $[H_2O_2]$ and $[Fe^{x+}]$ values the shorter the t_{99} value of the membrane. For the FER a reciprocal behaviour compared to t_{99} is visible. Thus, the calculated t_{99} and FER values are plotted and fitted with a reciprocal function (see Fig. 13). With this empirical correlation at hand, it is possible to estimate the t_{99} value based on the fluoride emission rate (averaged over 100 h).

Table 6 Calculated t_{99} and FER values (averaged over 100 h) for different conditions taken from the simulations above[33,35,36] (T = 368.15 K for all cases)

Conditions	t_{99}/h	FER/mol cm^{-2} h^{-1}
$[H_2O_2]$ = 4 mM $[Fe^{2+}]_0$ = 10 ppm	360	3.70×10^{-7}
$[H_2O_2]$ = 5.2 mM $[Fe^{2+}]_0$ = 6 ppm	460	5.15×10^{-8}
$[H_2O_2]$ = 3 mM $[Fe^{x+}]$ = 2.5 ppm, $[Fe^{2+}]_0/[Fe^{3+}]_0$ = 1	1920	2.86×10^{-8}
$[H_2O_2]$ = 0.5 mM $[Fe^{x+}]$ = 2.5 ppm, $[Fe^{2+}]_0/[Fe^{3+}]_0$ = 1	11 400	2.63×10^{-9}

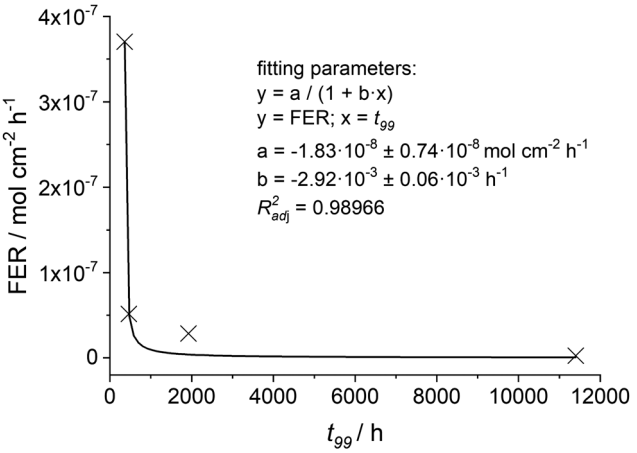

Fig. 13 The calculated fluoride emission rate (averaged over 100 h) is plotted as function of t_{99}. The crosses mark the four different conditions given in Table 6 and the black line indicates the fitted function.

Nevertheless, t_{99} should be considered as an upper limit of the membrane lifetime based on chemical degradation phenomena. It is expected to be further decreased by thermal and mechanical degradation. Yoon and Huang[93] performed gas-phase Fenton experiments, in which a Nafion® 212 membrane was conditioned with Fe^{x+} salts and subjected to gaseous H_2O_2 while keeping the membrane under mechanical stress. The authors observed an acceleration of chemical degradation.[93] In a similar study by Kusoglu *et al.*[94] (liquid-phase Fenton test of a compressed membrane), it was observed that the fluoride emission increases with the applied pressure. From these findings it was concluded that mechanical and chemical stressors act together, thereby influencing the kinetics of the degradation reactions.[94]

Mitigation of fuel cell degradation with cerium salts

To protect the chemical integrity of the membrane, two strategies are feasible: First, the input of transition metal contaminants and the amount of H_2O_2 produced during operation should be minimized. If this basic mitigation strategy is not possible, the number of reactive oxygen species can be reduced using radical scavengers. In the last two decades, various mitigation strategies have been investigated – an excellent overview is given in the review by Zatoń *et al.*[5]

Cerium serves either in its ionic form (Ce^{3+}, Ce^{4+})[41–44] or as solid cerium oxide (ceria, CeO_2)[45,46] as a radical scavenger. When ceria is incorporated into the membrane, it dissolves under operating conditions and produces both trivalent and tetravalent cerium ions.[45,99] A detailed scheme describing how CeO_2 mitigates membrane degradation by scavenging ROS was presented by Prabhakaran *et al.*[47] The most stable oxidation states +III and +IV form a redox couple ($E^0(Ce^{3+}/Ce^{4+})$ = −1.44 V

Open Access Article. Published on 26 February 2020. Downloaded on 2/15/2026 7:49:42 AM.
This article is licensed under a Creative Commons Attribution-NonCommercial 3.0 Unported Licence.

in 0.5 M or 1 M H_2SO_4[100]) rendering it a potent reactant in one-electron redox processes (*i.e.* quenching of radicals). The trivalent ion reacts with $^{\bullet}OH$ to form H_2O and Ce^{4+},[83] whereas the tetravalent ion reacts with H_2O_2 to regenerate Ce^{3+}.[95] Ce^{4+} is also known to oxidize Fe^{2+} to Fe^{3+};[98] hence the presence of tetravalent cerium ions slows down the Fenton reaction.[101] Table 7 gives an overview of the kinetic data for the reactions involving Ce^{x+} species.[45,83,95–98,102] Wong and Kjeang[45] estimated the same activation energy for reactions R_{24}–R_{27} in their model to describe the membrane degradation in ceria-supported fuel cells.

To study the influence of cerium scavengers on the ROS-initiated membrane degradation, the reactions from Table 7 were coupled to the main kinetic framework (Table 1). For a set of parameters ($[H_2O_2]$ = 1 mM, $[Fe^{2+}]_0$ = 5 ppm and T = 353.15 K) simulations with different concentrations of Ce^{3+} were performed (see Fig. 14). Per Ce^{3+} ion three protons in the membrane are displaced and thus, three sulfonic acid groups (BOL concentration 1.81 M) undergo complexation with Ce^{3+}.[41] It is clearly evident that Ce salts mitigate the destructive effects of the ROS. The higher the concentration of the cerium ions, the more ROS are quenched by the Ce^{3+}/Ce^{4+} system leading to lower fluoride emission rates and a smaller loss of hydrophilic head groups. When 30% of the SC–SO_3H sites are complexed with Ce^{3+} (at BOL), the FER (averaged over 100 h) is reduced by 2 orders of magnitude.

A situation similar to the dynamic equilibrium between the redox states of iron is evident for the cerium system. Simulations show that more than 99% of the cerium ions reside in the trivalent state and hence, are active for quenching $^{\bullet}OH$, the most destructive oxygen species. This is well in line with the modelling results by Gubler *et al.*[101] and Wong and Kjeang,[45,103] who also found that the dominant oxidation state in the cerium system is +III.

Coms *et al.*[41] incorporated Ce^{3+} ions (15% of SC–SO_3H complexed) into the membrane and found that the FER is reduced by 3 orders of magnitude (from 10^{-6} mol cm^{-2} h^{-1} to 1.6 × 10^{-9} mol cm^{-2} h^{-1}). When Ce^{3+} ions were introduced by spraying on both anode and cathode side (about 1% of SC–SO_3H complexed), the same FER value of 1.6 × 10^{-9} mol cm^{-2} h^{-1} was measured.[41] Similar results were presented by Zatoń *et al.*,[44] who observed a reduction of 2 orders of magnitude when loading the membrane with 0.04 mmol Ce^{3+} g^{-1} membrane.

The experimental results mentioned here demonstrate that Ce^{3+} ions are highly effective in protecting the chemical integrity of the membrane. In principle, the simulations illustrate the trend that higher $[Ce^{3+}]$ values lead to lower fluoride emission. However, the fact that at a ratio of complexation of 1% the FER drops by 3 orders of magnitude cannot satisfactorily be explained by the kinetic framework.

A fundamental assumption in the kinetic framework presented here is that all chemical species are distributed homogeneously throughout the membrane, though it is known that cerium ions migrate during the assembly and operation of the fuel cell. Stewart *et al.*[104] measured the cerium levels in

Table 7 Summary of kinetic data for reactions involving cerium species. For each reaction (R_{24}–R_{28}), rate constant k at 25 °C (= 298.15 K) in L mol^{-1} s^{-1}, activation energy E_a in kJ mol^{-1} and pre-exponential factor A in L mol^{-1} s^{-1} are given

Reaction			k (T = 298.15 K) [L mol^{-1} s^{-1}]	E_a [kJ mol^{-1}]	A [L mol^{-1} s^{-1}]
R_{24}	$Ce^{4+} + H_2O_2 \rightarrow Ce^{3+} + {}^{\bullet}OOH + H^+$	$r_{24} = k_{24}[Ce^{4+}][H_2O_2]$	$10^{6\,95}$	58[45 a]	1.45×10^{16}
R_{25}	$Ce^{4+} + {}^{\bullet}OOH \rightarrow Ce^{3+} + O_2 + H^+$	$r_{25} = k_{25}[Ce^{4+}][{}^{\bullet}OOH]$	$2.7 \times 10^{6\,95,96}$	58[45 a]	3.92×10^{16}
R_{26}	$Ce^{3+} + {}^{\bullet}OH + H^+ \rightarrow Ce^{4+} + H_2O$	$r_{26} = k_{26}[Ce^{3+}][{}^{\bullet}OH]$	$3 \times 10^{8\,83}$	58[45 a]	4.35×10^{18}
R_{27}	$Ce^{3+} + {}^{\bullet}OOH + H^+ \rightarrow Ce^{4+} + H_2O_2$	$r_{27} = k_{27}[Ce^{3+}][{}^{\bullet}OOH]$	$2.1 \times 10^{5\,97}$	58[45 a]	3.05×10^{15}
R_{28}	$Ce^{4+} + Fe^{2+} \rightarrow Fe^{3+} + Ce^{3+}$	$r_{28} = k_{28}[Ce^{4+}][Fe^{2+}]$	$1.3 \times 10^{6\,98}$	39.7	1.20×10^{13}

[a] For all four reactions the same activation energy is given in ref. 45.

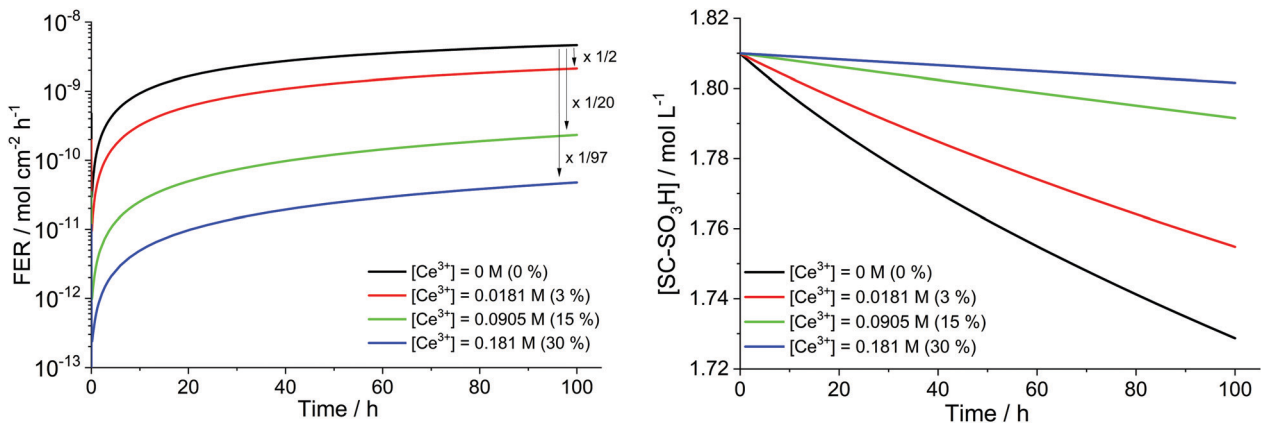

Fig. 14 Influence of trivalent cerium ion concentration ($[Ce^{3+}]$) in mol L^{-1} on the fluoride emission rate (left) and [SC–SO_3H] (right) for T = 353.15 K, $[H_2O_2]$ = 1 mM, $[Fe^{2+}]_0$ = 5 ppm. The arrows and numbers in the left graph indicate the reduction of the FER (averaged over 100 h). The values in the brackets correspond to the percentage of SC–SO_3H which are complexed by Ce^{3+} at BOL.

 This journal is © the Owner Societies 2020

Open Access Article. Published on 26 February 2020. Downloaded on 2/15/2026 7:49:42 AM.
This article is licensed under a Creative Commons Attribution-NonCommercial 3.0 Unported Licence.

Nafion® XL membranes, and found that the cerium level decreased from the BOL value of 7 μg cm^{-2} upon pressing and conditioning and subsequently during accelerated stress testing. The authors concluded that the cerium ions leave the membrane and enrich at both anode and cathode catalyst.[104] Zatoń *et al.*[44] also presented evidence that cerium migrates to the electrodes and is additionally eluted from the fuel cell, which limits the applicability of cerium scavengers in PEMFCs. Moreover, at increased Ce loadings (*e.g.* of SC–SO_3H complexed[41]) the performance of the fuel cell is also diminished.[41,43]

In addition to the reactions shown in Table 7 other pathways are also possible. A reduction of Ce^{4+} by H_2 or H_2O could also happen on Pt deposits in the membrane or Ce^{3+} can be oxidized by hydrogen radicals.[42] Under operating conditions, Ce^{4+} is also reduced to Ce^{3+} electrochemically.[45] Without doubt, these reactions influence the equilibrium of Ce^{3+} and Ce^{4+} and hence, also the radical scavenging.

Instead of using the expensive lanthanide cerium, a cheaper transition metal such as manganese can also be employed to quench ROS due to its rich redox chemistry.[41,44] A similar kinetic framework for manganese species was presented by Gubler *et al.*[101]

Conclusions

The zero-dimensional kinetic framework presented in this work allows to simulate chemical degradation phenomena in a fuel cell and (with caution) also under *ex situ* (Fenton) conditions. The kinetic framework relies on the assumption that the PFSA ionomer membrane in a fuel cell behaves like a 0D chemical reactor, and hence inhomogeneous distributions of chemical species are not covered here. Nevertheless, the said kinetic framework, which combines published data[14–28,33] and frameworks,[30–36] reproduces various sets of recent experimental data[33,35–37] (concentrations of ionomer moieties and FERs). To account for effects like additional sources of radicals[73–75] or the potential-dependent redox recycling of iron species,[34] the used Fe^{x+} and H_2O_2 concentrations might be higher than in a real fuel cell under working or OCV conditions.

At the core of the model is the Fenton reaction between hydrogen peroxide and Fe^{2+}, which leads to the formation of hydroxyl radicals. The role of the Pt catalyst or Pt deposits in the membrane in the overall degradation is not considered in this kinetic framework. This is mainly due to the fact that the dimensionality of the reactor model conflicts with processes happening at phase boundaries such as Pt surfaces, which request a higher dimensionality of the model and the implementation of diffusive processes. The implications of Pt catalyst for the chemical membrane degradation will be addressed in an upcoming publication.

Instead of Pt, the involvement of alternative ORR catalysts in membrane degradation is outlined. Such catalysts offer in principle a cheap, though effective, replacement for precious Pt; however, the demetallation in the case of Fe–N–C should be regarded with care. Leaching of iron species from the catalyst (or other constituents of the fuel cell system) in combination with hydrogen peroxide poses a major threat to the chemical integrity of the membrane. Thus, is it imperative to minimize the Fe contamination and the input of additional Fe species into the system. Not only iron species, but also other metal species like Ti^{3+},[66] Co^{2+} [68,69] or Cu^{+} [70–72] are known to produce ROS. This should be borne in mind when developing and testing new materials and catalysts to be used in PEMFC systems.

Since Fe is present in both the +II and +III oxidation states in our kinetic framework, the interplay of ferrous and ferric ions (redox recycling) was investigated. Interestingly, the simulation results (concentration traces, FERs) do not depend on the oxidation state of Fe at $t = 0$. It was found that a dynamic equilibrium between both oxidation states of iron is established rather rapidly (within several seconds), compared to the long simulation times (usually 100 hours). In this dynamic equilibrium 99% of the iron resides in the +III state (*i.e.* the Fenton-inactive redox state), which greatly decelerates the degradation of the membrane. For a real PEMFC system, a potential-dependent redox recycling of Fenton-active iron species was proposed by Wong and Kjeang.[34] The authors found in their simulations that the fluoride emission is lowered when the system is operated at voltages below 0.7 V, as $[Fe^{2+}]$ is decreased.

In an approach to describe membrane lifetimes the parameter t_{99} was introduced. It represents the time necessary to degrade 99% of all sulfonic acid head groups. A reciprocal correlation between this calculated parameter and the average FER was found. Hence, it is possible to predict chemical membrane lifetimes (or to be more precise, an upper limit) from FER values, which are accessible by experiment. Degradation phenomena of thermal and mechanical nature[5–7] are not considered here. It can be expected that these degradation mechanisms lower the lifetime based on chemical degradation, as mechanical stress exacerbates the damage induced by chemical stressors.[93,94]

To demonstrate the facile expandability of the kinetic framework, five additional equations describing reactions of H_2O_2, ROS and Fe^{2+} with cerium ions, which act as radical quenchers, are coupled to the main framework. Simulations with the expanded framework show that the addition of cerium ions to the membrane reduces the loss of sulfonic acid head groups and decreases the fluoride emission. Yet, the fact that the FER is reduced by 3 orders of magnitude, when about 1% of all sulfonic acid groups are complexed with Ce^{3+},[41] cannot be explained satisfactorily by the extended 0D reactor model. A reduction of the FER by 2 orders of magnitude is observed when 30% of all SC–SO_3H groups are complexed with Ce^{3+} (at BOL).

We have developed a routine providing extensive data sets in a short amount of time. Graphical representations generated by the *copd* routine *via gnuplot* allow a fast assessment of the data prior to further manipulation of data. A web interface of the kinetic framework is available under http://ptc-pc-139.tugraz.at/cgi-bin/Membrane_Degradation/.

Open Access Article. Published on 26 February 2020. Downloaded on 2/15/2026 7:49:42 AM.
This article is licensed under a Creative Commons Attribution-NonCommercial 3.0 Unported Licence.

In the future, further steps to explore the connection between simulated and experimental data will be undertaken. To do so, the 0D chemical reactor model will be integrated into a more extensive fuel cell degradation model.

Conflicts of interest

There are no conflicts to declare.

Acknowledgements

Financial support by the Austrian Research Promotion Agency (FFG; project number: 854867) is gratefully acknowledged. This work is part of the SoH4PEM (State of Health Monitoring for Proton Exchange Membrane Fuel Cell Stacks) project. The research is partially funded by the Slovenian Research Agency (research core funding no. P2-0401).

Notes and references

1 I. Staffell, D. Scamman, A. Velazquez Abad, P. Balcombe, P. E. Dodds, P. Ekins, N. Shah and K. R. Ward, *Energy Environ. Sci.*, 2019, **12**, 463–491.
2 T. Wilberforce, Z. El-Hassan, F. N. Khatib, A. Al Makky, A. Baroutaji, J. G. Carton and A. G. Olabi, *Int. J. Hydrogen Energy*, 2017, **42**, 25695–25734.
3 R. J. Detz, J. N. H. Reek and B. C. C. van der Zwaan, *Energy Environ. Sci.*, 2018, **11**, 1653–1669.
4 M. R. Shaner, H. A. Atwater, N. S. Lewis and E. W. McFarland, *Energy Environ. Sci.*, 2016, **9**, 2354–2371.
5 M. Zatoń, J. Rozière and D. J. Jones, *Sustainable Energy Fuels*, 2017, **1**, 409–438.
6 R. Borup, J. Meyers, B. Pivovar, Y. S. Kim, R. Mukundan, N. Garland, D. Myers, M. Wilson, F. Garzon, D. Wood, P. Zelenay, K. More, K. Stroh, T. Zawodzinski, J. Boncella, J. E. McGrath, M. Inaba, K. Miyatake, M. Hori, K. Ota, Z. Ogumi, S. Miyata, A. Nishikata, Z. Siroma, Y. Uchimoto, K. Yasuda, K. Kimijima and N. Iwashita, *Chem. Rev.*, 2007, **107**, 3904–3951.
7 A. Kusoglu and A. Z. Weber, *Chem. Rev.*, 2017, **117**, 987–1104.
8 A. Collier, H. Wang, X. Z. Yuan, J. Zhang and D. P. Wilkinson, *Int. J. Hydrogen Energy*, 2006, **31**, 1838–1854.
9 D. E. Curtin, R. D. Lousenberg, T. J. Henry, P. C. Tangeman and M. E. Tisack, *J. Power Sources*, 2004, **131**, 41–48.
10 F. D. Coms, *ECS Transactions*, ECS, 2008, vol. 16, pp. 235–255.
11 L. Ghassemzadeh, K.-D. Kreuer, J. Maier and K. Müller, *J. Phys. Chem. C*, 2010, **114**, 14635–14645.
12 L. Ghassemzadeh and S. Holdcroft, *J. Am. Chem. Soc.*, 2013, **135**, 8181–8184.
13 L. Ghassemzadeh, T. J. Peckham, T. Weissbach, X. Luo and S. Holdcroft, *J. Am. Chem. Soc.*, 2013, **135**, 15923–15932.
14 F. S. Dainton and J. Rowbottom, *Trans. Faraday Soc.*, 1953, **49**, 1160–1173.
15 T. Rigg, W. Taylor and J. Weiss, *J. Chem. Phys.*, 1954, **22**, 575–577.
16 T. Lundström, H. Christensen and K. Sehested, *Radiat. Phys. Chem.*, 2001, **61**, 109–113.
17 Y. Lee, C. Lee and J. Yoon, *Chemosphere*, 2003, **51**, 963–971.
18 C. Lee and J. Yoon, *Chemosphere*, 2004, **56**, 923–934.
19 T. Lundström, H. Christensen and K. Sehested, *Radiat. Phys. Chem.*, 2004, **69**, 211–216.
20 A. M. Dreizler and E. Roduner, *Fuel Cells*, 2012, **12**, 132–140.
21 P. A. Giguère and I. D. Liu, *Can. J. Chem.*, 1957, **35**, 283–293.
22 C. Walling and A. Goosen, *J. Am. Chem. Soc.*, 1973, **95**, 2987–2991.
23 G. G. Jayson, B. J. Parsons and A. J. Swallow, *J. Chem. Soc., Faraday Trans. 1*, 1973, **69**, 236–242.
24 B. H. J. Bielski, *Photochem. Photobiol.*, 1978, **28**, 645–649.
25 H. Christensen and K. Sehested, *Radiat. Phys. Chem.*, 1981, **18**, 723–731.
26 H. Christensen, K. Sehested and H. Corfitzen, *J. Phys. Chem.*, 1982, **86**, 1588–1590.
27 H. Christensen and K. Sehested, *J. Phys. Chem.*, 1983, **87**, 118–120.
28 P. Maruthamuthu, S. Padmaja and R. E. Huie, *Int. J. Chem. Kinet.*, 1995, **27**, 605–612.
29 T. Xie and C. A. Hayden, *Polymer*, 2007, **48**, 5497–5506.
30 A. A. Shah, T. R. Ralph and F. C. Walsh, *J. Electrochem. Soc.*, 2009, **156**, B465–B484.
31 L. Gubler, S. M. Dockheer and W. H. Koppenol, *J. Electrochem. Soc.*, 2011, **158**, B755–B769.
32 M. Ghelichi, P.-É. A. Melchy and M. H. Eikerling, *J. Phys. Chem. B*, 2014, **118**, 11375–11386.
33 K. H. Wong and E. Kjeang, *J. Electrochem. Soc.*, 2014, **161**, F823–F832.
34 K. H. Wong and E. Kjeang, *ChemSusChem*, 2015, **8**, 1072–1082.
35 R. Singh, P. C. Sui, K. H. Wong, E. Kjeang, S. Knights and N. Djilali, *J. Electrochem. Soc.*, 2018, **165**, F3328–F3336.
36 G. A. Futter, A. Latz and T. Jahnke, *J. Power Sources*, 2019, **410–411**, 78–90.
37 V. A. Sethuraman, J. W. Weidner, A. T. Haug and L. V. Protsailo, *J. Electrochem. Soc.*, 2008, **155**, B119–B124.
38 D. Banham, S. Ye, K. Pei, J. Ozaki, T. Kishimoto and Y. Imashiro, *J. Power Sources*, 2015, **285**, 334–348.
39 C. H. Choi, C. Baldizzone, G. Polymeros, E. Pizzutilo, O. Kasian, A. K. Schuppert, N. Ranjbar Sahraie, M.-T. Sougrati, K. J. J. Mayrhofer and F. Jaouen, *ACS Catal.*, 2016, **6**, 3136–3146.
40 R. Chenitz, U. I. Kramm, M. Lefèvre, V. Glibin, G. Zhang, S. Sun and J.-P. Dodelet, *Energy Environ. Sci.*, 2018, **11**, 365–382.
41 F. D. Coms, H. Liu and J. E. Owejan, *ECS Transactions*, ECS, 2008, vol. 16, pp. 1735–1747.
42 M. Danilczuk, S. Schlick and F. D. Coms, *Macromolecules*, 2009, **42**, 8943–8949.
43 A. M. Baker, R. Mukundan, D. Spernjak, E. J. Judge, S. G. Advani, A. K. Prasad and R. L. Borup, *J. Electrochem. Soc.*, 2016, **163**, F1023–F1031.

Open Access Article. Published on 26 February 2020. Downloaded on 2/15/2026 7:49:42 AM.
This article is licensed under a Creative Commons Attribution-NonCommercial 3.0 Unported Licence.

44 M. Zatoń, B. Prélot, N. Donzel, J. Rozière and D. J. Jones, *J. Electrochem. Soc.*, 2018, **165**, F3281–F3289.
45 K. H. Wong and E. Kjeang, *J. Electrochem. Soc.*, 2017, **164**, F1179–F1186.
46 B. P. Pearman, N. Mohajeri, R. P. Brooker, M. P. Rodgers, D. K. Slattery, M. D. Hampton, D. A. Cullen and S. Seal, *J. Power Sources*, 2013, **225**, 75–83.
47 V. Prabhakaran, C. G. Arges and V. Ramani, *Proc. Natl. Acad. Sci. U. S. A.*, 2012, **109**, 1029–1034.
48 A. Panchenko, H. Dilger, E. Möller, T. Sixt and E. Roduner, *J. Power Sources*, 2004, **127**, 325–330.
49 M. Danilczuk, F. D. Coms and S. Schlick, *J. Phys. Chem. B*, 2009, **113**, 8031–8042.
50 H. S. Wroblowa, Y.-C. Pan and G. Razumney, *J. Electroanal. Chem. Interfacial Electrochem.*, 1976, **69**, 195–201.
51 A. M. Gómez-Marín, R. Rizo and J. M. Feliu, *Catal. Sci. Technol.*, 2014, **4**, 1685–1698.
52 W. Liu and D. Zuckerbrod, *J. Electrochem. Soc.*, 2005, **152**, A1165–A1170.
53 C. Chen and T. Fuller, *ECS Transactions*, ECS, 2007, vol. 11, pp. 1127–1137.
54 M. Inaba, T. Kinumoto, M. Kiriake, R. Umebayashi, A. Tasaka and Z. Ogumi, *Electrochim. Acta*, 2006, **51**, 5746–5753.
55 H. J. H. Fenton, *J. Chem. Soc., Trans.*, 1894, **65**, 899–910.
56 G. Ruppert, R. Bauer and G. Heisler, *J. Photochem. Photobiol., A*, 1993, **73**, 75–78.
57 A. Pozio, R. F. Silva, M. De Francesco and L. Giorgi, *Electrochim. Acta*, 2003, **48**, 1543–1549.
58 W. G. Barb, J. H. Baxendale, P. George and K. R. Hargrave, *Trans. Faraday Soc.*, 1951, **47**, 462–500.
59 W. G. Barb, J. H. Baxendale, P. George and K. R. Hargrave, *Trans. Faraday Soc.*, 1951, **47**, 591–616.
60 D. D. Papadias, R. K. Ahluwalia, J. K. Thomson, H. M. Meyer, M. P. Brady, H. Wang, J. A. Turner, R. Mukundan and R. Borup, *J. Power Sources*, 2015, **273**, 1237–1249.
61 F. D. Coms, S. Schlick and M. Danilczuk, in *The Chemistry of Membranes Used in Fuel Cells: Degradation and Stabilization*, ed. S. Schlick, John Wiley & Sons, Inc., Hoboken, NJ, USA, 2018, pp. 75–106.
62 H. Liu, J. Zhang, F. D. Coms, W. Gu, B. Litteer and H. A. Gasteiger, *ECS Transactions*, ECS, 2006, vol. 3, pp. 493–505.
63 P. Maletzky, R. Bauer, J. Lahnsteiner and B. Pouresmael, *Chemosphere*, 1999, **38**, 2315–2325.
64 S. M. Andersen, *J. Fuel Cell Sci. Technol.*, 2016, **12**, 061010.
65 C. Walling, *Acc. Chem. Res.*, 1975, **8**, 125–131.
66 A. Bosnjakovic and S. Schlick, *J. Phys. Chem. B*, 2004, **108**, 4332–4337.
67 L. Ghassemzadeh, K. D. Kreuer, J. Maier and K. Müller, *J. Power Sources*, 2011, **196**, 2490–2497.
68 M. B. Kadiiska, K. R. Maples and R. P. Mason, *Arch. Biochem. Biophys.*, 1989, **275**, 98–111.
69 P. M. Hanna, M. B. Kadiiska and R. P. Mason, *Chem. Res. Toxicol.*, 1992, **5**, 109–115.
70 J. W. Moffett and R. G. Zika, *Environ. Sci. Technol.*, 1987, **21**, 804–810.
71 F. J. Millero, V. K. Sharma and B. Karn, *Mar. Chem.*, 1991, **36**, 71–83.
72 A. D. Bokare and W. Choi, *J. Hazard. Mater.*, 2014, **275**, 121–135.
73 V. Atrazhev, E. N. Timokhina, S. F. Burlatsky, V. I. Sultanov, T. H. Madden and M. Gummalla, *ECS Transactions*, ECS, 2008, vol. 6, pp. 69–74.
74 D. Zhao, B. L. Yi, H. M. Zhang and M. Liu, *J. Power Sources*, 2010, **195**, 4606–4612.
75 M. P. Rodgers, B. P. Pearman, L. J. Bonville, D. A. Cullen, N. Mohajeri and D. K. Slattery, *J. Electrochem. Soc.*, 2013, **160**, F1123–F1128.
76 M. I. Bro and C. A. Sperati, *J. Polym. Sci.*, 1959, **38**, 289–295.
77 K. E. Schwiebert, K. G. Raiford, G. Escobedo and G. Nagarajan, *ECS Transactions*, ECS, 2006, vol. 1, pp. 303–311.
78 C. Zhou, M. A. Guerra, Z.-M. Qiu, T. A. Zawodzinski and D. A. Schiraldi, *Macromolecules*, 2007, **40**, 8695–8707.
79 N. E. Cipollini, *ECS Transactions*, ECS, 2007, vol. 11, pp. 1071–1082.
80 M. Danilczuk, A. J. Perkowski and S. Schlick, *Macromolecules*, 2010, **43**, 3352–3358.
81 M. K. Kadirov, A. Bosnjakovic and S. Schlick, *J. Phys. Chem. B*, 2005, **109**, 7664–7670.
82 A. Bosnjakovic, M. K. Kadirov and S. Schlick, *Res. Chem. Intermed.*, 2007, **33**, 677–687.
83 G. V. Buxton, C. L. Greenstock, W. P. Helman and A. B. Ross, *J. Phys. Chem. Ref. Data*, 1988, **17**, 513–886.
84 T. Tokumasu, I. Ogawa, M. Koyama, T. Ishimoto and A. Miyamoto, *J. Electrochem. Soc.*, 2011, **158**, B175–B179.
85 S. Hoops, S. Sahle, R. Gauges, C. Lee, J. Pahle, N. Simus, M. Singhal, L. Xu, P. Mendes and U. Kummer, *Bioinformatics*, 2006, **22**, 3067–3074.
86 T. Madden, D. Weiss, N. Cipollini, D. Condit, M. Gummalla, S. Burlatsky and V. Atrazhev, *J. Electrochem. Soc.*, 2009, **156**, B657–B662.
87 Y. Zhao, M. Yamaguchi, E. Tsuchida, Y.-K. Choe and T. Ikeshoji, *J. Phys. Chem. C*, 2018, **122**, 20135–20143.
88 J. D. Rush and B. H. J. Bielski, *J. Phys. Chem.*, 1985, **89**, 5062–5066.
89 G. G. Jayson, B. J. Parsons and A. J. Swallow, *J. Chem. Soc., Faraday Trans. 1*, 1972, **68**, 2053–2058.
90 V. A. Sethuraman, J. W. Weidner, A. T. Haug, S. Motupally and L. V. Protsailo, *J. Electrochem. Soc.*, 2008, **155**, B50–B57.
91 C. Lim, L. Ghassemzadeh, F. Van Hove, M. Lauritzen, J. Kolodziej, G. G. Wang, S. Holdcroft and E. Kjeang, *J. Power Sources*, 2014, **257**, 102–110.
92 M. Chandesris, R. Vincent, L. Guetaz, J.-S. Roch, D. Thoby and M. Quinaud, *Int. J. Hydrogen Energy*, 2017, **42**, 8139–8149.
93 W. Yoon and X. Huang, *ECS Transactions*, 2010, vol. 33, pp. 907–911.
94 A. Kusoglu, M. Calabrese and A. Z. Weber, *ECS Electrochem. Lett.*, 2014, **3**, F33–F36.
95 G. Czapski, B. H. J. Bielski and N. Sutin, *J. Phys. Chem.*, 1963, **67**, 201–203.
96 B. H. J. Bielski, D. E. Cabelli, R. L. Arudi and A. B. Ross, *J. Phys. Chem. Ref. Data*, 1985, **14**, 1041–1100.

Open Access Article. Published on 26 February 2020. Downloaded on 2/15/2026 7:49:42 AM.
This article is licensed under a Creative Commons Attribution-NonCommercial 3.0 Unported Licence.

97 D. Meisel, Y. A. Ilan and G. Czapski, *J. Phys. Chem.*, 1974, **78**, 2330–2334.
98 G. Dulz and N. Sutin, *Inorg. Chem.*, 1963, **2**, 917–921.
99 S. A. Hayes, P. Yu, T. J. O'Keefe, M. J. O'Keefe and J. O. Stoffer, *J. Electrochem. Soc.*, 2002, **149**, C623–C630.
100 E. Wadsworth, F. R. Duke and C. A. Goetz, *Anal. Chem.*, 1957, **29**, 1824–1825.
101 L. Gubler and W. H. Koppenol, *J. Electrochem. Soc.*, 2011, **159**, B211–B218.
102 T. J. Sworski, H. A. Mahlman and R. W. Matthews, *J. Phys. Chem.*, 1971, **75**, 250–255.
103 K. H. Wong and E. Kjeang, *J. Electrochem. Soc.*, 2019, **166**, F128–F136.
104 S. M. Stewart, D. Spernjak, R. Borup, A. Datye and F. Garzon, *ECS Electrochem. Lett.*, 2014, **3**, F19–F22.

This journal is © the Owner Societies 2020